

Article

# Geological, Geochronological, and Geochemical Insights into the Formation of the Giant Pulang Porphyry Cu (–Mo–Au) Deposit in Northwestern Yunnan Province, SW China

Qun Yang <sup>1</sup>, Yun-Sheng Ren <sup>1,2,\*</sup>, Sheng-Bo Chen <sup>3</sup>, Guo-Liang Zhang <sup>4</sup>, Qing-Hong Zeng <sup>3</sup>, Yu-Jie Hao <sup>2</sup>, Jing-Mou Li <sup>1</sup>, Zhong-Jie Yang <sup>5</sup>, Xin-Hao Sun <sup>1</sup> and Zhen-Ming Sun <sup>1</sup>

- <sup>1</sup> College of Earth Sciences, Jilin University, Changchun 130061, China; yangq2009@jlu@163.com (Q.Y.); Lijmmy2019@163.com (J.-M.L.); xhsun17@mails.jlu.edu.cn (X.-H.S.); sunzhenming.9040@163.com (Z.-M.S.)
- <sup>2</sup> Key Laboratory of Mineral Resources Evaluation in Northeast Asia, Ministry of Natural Resources of China, Changchun 130026, China; haoyujie@jlu.edu.cn
- <sup>3</sup> College of Geo-Exploration Science and Technology, Jilin University, Changchun 130026, China; chensb@jlu.edu.cn (S.-B.C.); zengqh17@mails.jlu.edu.cn (Q.-H.Z.)
- <sup>4</sup> Key Laboratory of Satellite Remote Sensing Application Technology of Jilin Province, Chang Guang Satellite Technology Co., Ltd., Changchun 130102, China; zhanggl0207@163.com
- <sup>5</sup> Geological Survey Institute of Liaoning Province, Shenyang 110031, China; yangzj870227@163.com
- \* Correspondence: renys@jlu.edu.cn; Tel: +86-0431-88502708

Received: 7 March 2019; Accepted: 19 March 2019; Published: 21 March 2019



**Abstract:** The giant Pulang porphyry Cu (–Mo–Au) deposit in Northwestern Yunnan Province, China, is located in the southern part of the Triassic Yidun Arc. The Cu orebodies are mainly hosted in quartz monzonite porphyry (QMP) intruding quartz diorite porphyry (QDP) and cut by granodiorite porphyry (GP). New LA-ICP-MS zircon U–Pb ages indicate that QDP ( $227 \pm 2$  Ma), QMP ( $218 \pm 1$  Ma,  $219 \pm 1$  Ma), and GP ( $209 \pm 1$  Ma) are significantly different in age; however, the molybdenite Re–Os isochron age ( $218 \pm 2$  Ma) indicates a close temporal and genetic relationship between Cu mineralization and QMP. Pulang porphyry intrusions are enriched in light rare-earth elements (LREEs) and large ion lithophile elements (LILEs), and depleted in heavy rare-earth elements (HREEs) and high field-strength elements (HFSEs), with moderately negative Eu anomalies. They are high in SiO<sub>2</sub>, Al<sub>2</sub>O<sub>3</sub>, Sr, Na<sub>2</sub>O/K<sub>2</sub>O, Mg#, and Sr/Y, but low in Y, and Yb, suggesting a geochemical affinity to high-silica (HSA) adakitic rocks. These features are used to infer that the Pulang HSA porphyry intrusions were derived from the partial melting of a basaltic oceanic-slab. These magmas reacted with peridotite during their ascent through the mantle wedge. This is interpreted to indicate that the Pulang Cu deposit and associated magmatism can be linked to the synchronous westward subduction of the Ganzi–Litang oceanic lithosphere, which has been established as Late Triassic.

**Keywords:** Pulang porphyry Cu (–Mo–Au) deposit; LA-ICP-MS zircon U–Pb dating; molybdenite Re–Os dating; high-silica adakitic rocks (HSA); Northwestern Yunnan Province

## 1. Introduction

Two famous porphyry mineralization systems in Western Yunnan Province, Southwestern (SW) China, mainly compose the Yidun Arc metallogenic belt in the north and the Jinshajiang–Red River metallogenic belt in the south (Figure 1A). The southern Yidun Arc (Figure 1B), namely, the Zhongdian Arc, is important for its Cu resources. Numerous porphyry and skarn Cu deposits have been discovered in the area, and representative deposits include Pulang, Xuejiping, Lannitang, Songnuo, Langdu, and Chundu (Figure 1C). The geological characteristics and geochronological data indicate that these

Cu deposits have a temporal and spatial relationship with widespread Mesozoic intermediate-acid intrusions [1–9]. Recently, extensive isotopic geochronology studies have been carried out on these Cu deposits. Cu mineralization ages in the southern Yidun Arc have now been constrained to the Late Triassic period (210–230 Ma) by zircon U–Pb and molybdenite Re–Os dating [5–13].

The Pulang deposit, located ~36 km northeast of the Shangri-La County in Northwestern Yunnan Province, is one of the large-scale porphyry Cu (–Mo–Au) deposits in China. It is located in the Sanjiang Tethyan metallogenic domain in Yunnan Province, SW China, and contains reserves of 4.18 Mt Cu. The largest KT1 orebody contains reserves of 1.57 Mt Cu @ 0.52%, 54t Au @ 0.18g/t, and 84,800 t Mo @ 0.01% [14]. In the past ten years, because of its giant size, the deposit has attracted much attention, especially regarding its ore geology [15–17], geochronology, and petro-geochemistry [18–23]. Despite the existing geochronological and geochemical studies on the Pulang Cu deposit, there remains an insufficient understanding on the accurate diagenesis and mineralization ages, the relationships between Cu mineralization and associated magmatism, and the tectonic setting. To start with, the mineralization age of Pulang deposit is still a matter of debate, as the limited molybdenite Re–Os age ranging from  $208 \pm 15$  Ma to  $213 \pm 4$  Ma [3,18,24] is a substantial margin of error. Next, the published geochronological data for the quartz monzonite porphyry (QMP) and quartz diorite porphyry (QDP) in the Pulang deposit are in a broad range of 211–231 Ma and 214–228 Ma, respectively [4–6,10,18,19,22,23]. Some of these ages are younger than the Re–Os isochron ages of molybdenite [4,5,14,19], whereas some are ~15 Ma older than the Re–Os isochron ages of molybdenite [22,25]. Generally, a porphyry-type hydrothermal Cu mineralization system lasts for less than 10 Ma [26]. Therefore, most of these ages are not well explained in relation to the observed Cu mineralization. In addition, the relationship between Cu mineralization and associated magmatism remains unclear and controversial as a result of the ~20 Ma age interval (210–230 Ma) for the Pulang porphyry intrusions. Some scholars have considered the QMP to be the ore-causative intrusion [18,23], whereas others have deemed that all of the Pulang porphyry intrusions contributed to Cu mineralization [14,27,28]. Finally, there are also divergences in the understanding of the petrogenesis of these ore-bearing porphyries; some scholars have proposed that the Pulang porphyries associated with Cu mineralization are related to the partial melting of the Ganzi-Litang oceanic plate [10,13], while others have considered the formation of these porphyries to be related to the partial melting of enriched mantle and the assimilation and fractional crystallization (AFC) of mantle-derived basalt magma [14,27].

To address these issues, this study presents new zircon U–Pb geochronology and whole-rock major-trace elemental data for Pulang porphyry intrusions and molybdenite Re–Os ages for different types of ore. The aim of the study is to provide precise diagenesis and mineralization ages, explain the relationship between associated intrusions and Cu mineralization, evaluate the contribution of Pulang porphyry intrusions to the Cu mineralization, and discuss the geodynamic setting of the intrusions and associated Cu mineralization in the Pulang Cu (–Mo–Au) deposit.

## 2. Geological Background

The NNW-trending Yidun terrane is located between the Garze–Litang Suture and the Jinshajiang Suture (Figure 1B), which represent closure zones of two distinct Paleo-Tethys oceans during the Middle–Late Triassic and Late Paleozoic, respectively [29–31]. The Yidun Terrane is divided into the Zhongza Massif in the west and the Yidun Arc in the east by the NS-trending Xiangchang–Geza fault [32,33]. The subduction of the Garze–Litang oceanic plate beneath the Zhongza Block resulted in the accretion of the Zhongza Block to the Yangtze Craton via the Yidun Arc during the Late Triassic time. It is inferred that the Yidun Arc developed on the basement that was inherited from the Yangtze Craton [14].

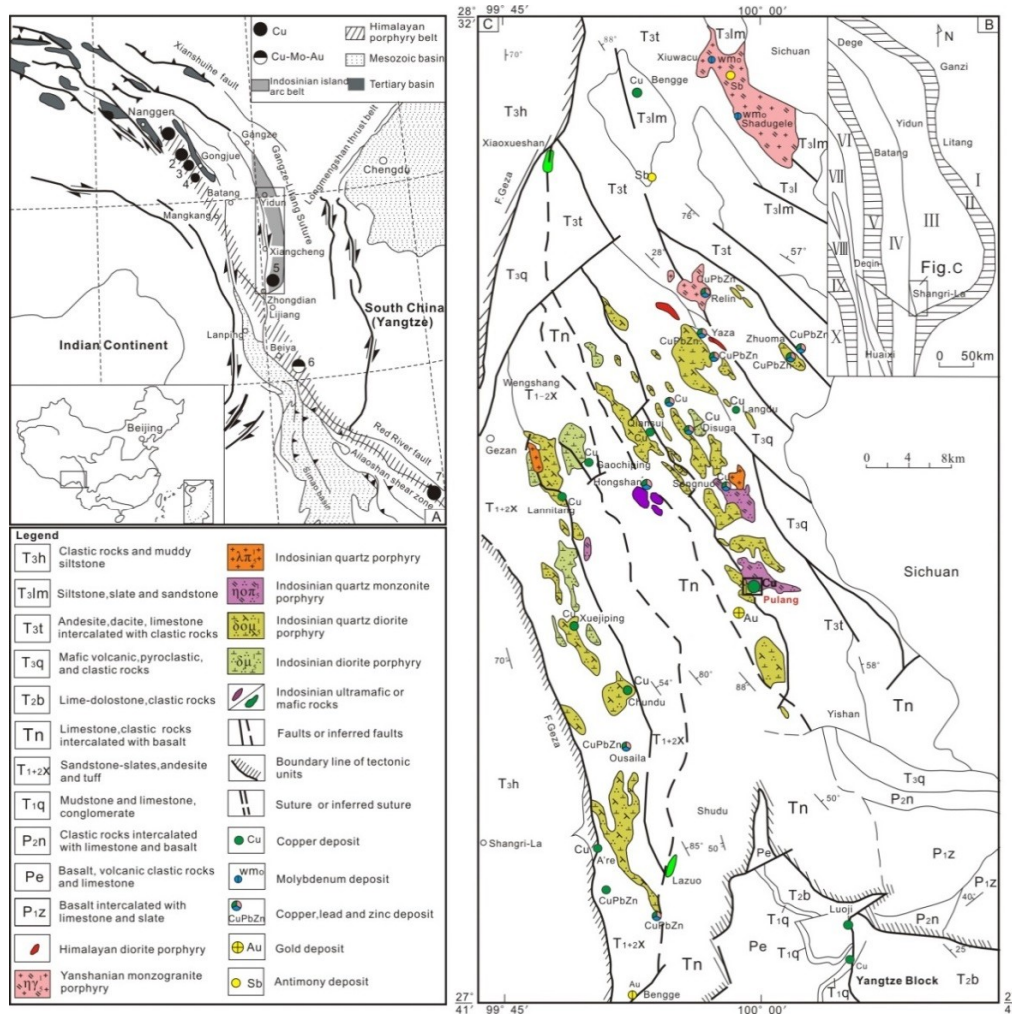


**Figure 1.** (A) Regional tectonic map of the Zhongdian island-arc zone (based on Li et al. [20]), showing the Indosinian and Himalayan porphyry Cu belts and deposits numbered as follows: 1 = Yulong; 2 = Malasongsuo; 3 = Duoxiasongsuo; 4 = Mamupu; 5 = Pulang; 6 = Machangqing; 7 = Tongchang. (B) Tectonic location map and (C) regional geology map of the Pulang Cu deposit (based on Wang et al. [34]). I = Yangtze block; II = Garze–Litang suture zone; III = Yidun arc belt; IV = Zhongza block; V = Jinsahjiang suture zone; VI = Jomda–Weixi magmatic arc; VII = Changdu–Lanping block; VIII = Sandashan–Jinghong volcanic arc; IX = Lancangjiang suture zone; X = Baoshan block.

The Yidun Arc is almost entirely overlain by the Triassic Yidun Group, which consists of slate, sandstone interbedded with minor limestone and flysch–volcanic succession, and intrusive rocks, which were produced by the westward subduction of the Garze–Litang oceanic plate (Figure 1C) [35,36]. Structures in the area are dominated by the NW–SE-trending or N–S-trending regional faults associated with the subduction, which channeled the NW–SE-trending Mesozoic intrusions (Figure 1C). The subduction-related magmatism resulted in abundant calc-alkaline arc-related volcanic rocks (such as andesite, rhyolite, and basalt), which developed at ~230 Ma in the northern segment of the Yidun Arc, and the voluminous Late Triassic (206–237 Ma) intermediate to felsic porphyritic rocks (such as quartz porphyry, quartz monzonite porphyry, quartz diorite porphyry, and diorite porphyry) in the southern segment of the Yidun Arc (Zhongdian Arc) [20,37].

Volcanic-associated massive sulfide (VMS) deposits, such as the Gayiqiong Zn–Pb–Cu, Shengmolong Zn–Pb, and Gacun giant Zn–Pb–Ag–Cu deposits, are distributed in the northern segment of the Yidun Arc, whereas abundant economic porphyry Cu deposits, such as the well-known Pulang, Xuejiping, Lannitang, and Chundu deposits, are mainly distributed in the southern segment of the

Yidun Arc (Figure 1C) [20,33]. The different types of deposits in the northern and southern segment of the Yidun Arc are probably attributable to the subduction angle of the Garze–Litang oceanic plate in the Middle–Late Triassic [20,33]. As a result of a steep subduction angle, the northern segment of the Yidun Arc was tensional, which induced magma spill over onto the surface and caused extensive volcanic rocks to accompany the formation of some volcanic massive sulfide-type deposits. By contrast, owing to a gentle angle of subduction, the southern segment of the Yidun Arc was compressional, which caused the magma to remain below the surface and formed hypabyssal porphyritic intrusions related to porphyry-type deposits.

### 3. Deposit Geology

The Pulang porphyry Cu (–Mo–Au) ore district (Location: 28°02′19″ N, 99°59′23″ E) is situated ~36 km northeast of the Shangri-La (Zhongdian) County in Northwestern Yunnan Province (Figure 1C). It contains the largest ore block with ~96% of the total ore reserves in the south and smaller ore blocks in the north and east. Besides minor Quaternary strata, the ore district mainly consists of the Late Triassic Tumugou Formation and large-scale porphyry intrusions over an area of 8.9 km<sup>2</sup> (Figure 2A). The Tumugou Formation consists of interlayered slates and sandstones, minor limestones, and volcanic rocks. NW-trending Heishuitang and NEE-trending Quanganlida faults controlled the porphyry intrusions and the major Cu orebodies [28].

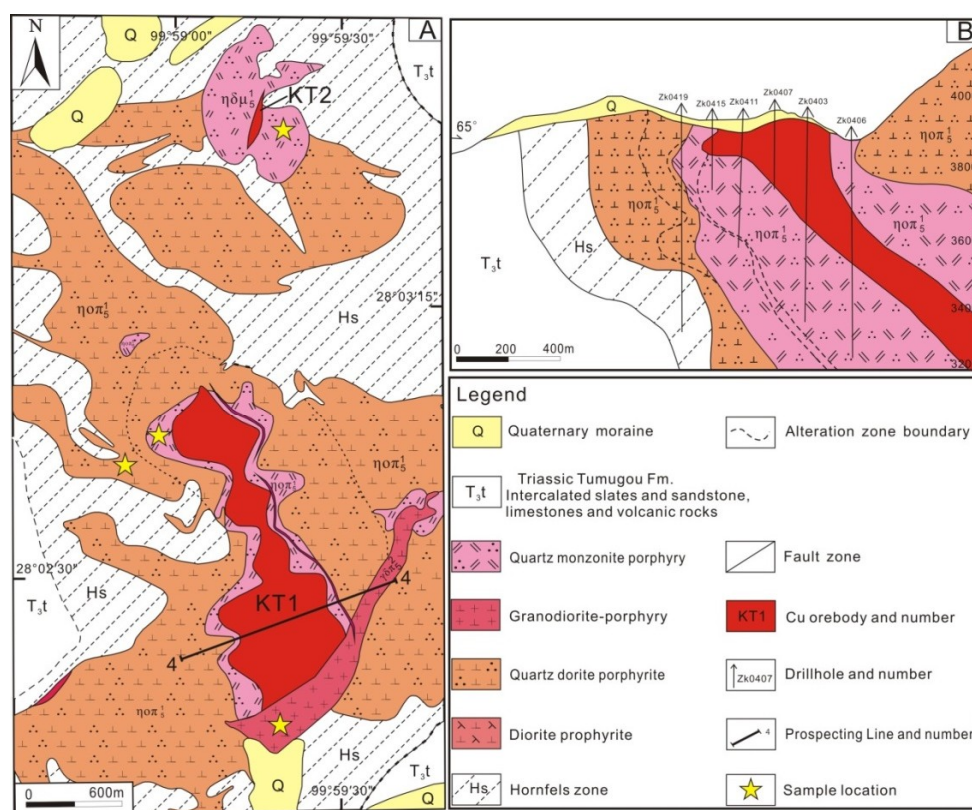


**Figure 2.** (A) Geological map of the Pulang porphyry Cu (–Mo–Au) deposit showing the biggest orebody KT1 and KT2 (based on Wang et al. [14]). (B) Geological section of the No. 4 exploration line in the Pulang porphyry Cu (–Mo–Au) deposit (based on Li et al. [20]).

The intrusive units in Pulang occurred mainly as NW-trending porphyry intrusions that can be grouped into three types on the basis of their cross-cutting relationship and petrographic characteristics. The quartz diorite porphyry (QDP) forms the largest intrusion and is widespread in the ore district. The QMP is the most important ore-hosting intrusion, and it trends mainly NNW–SSE within the QDP in the southern part of the ore district (Figure 2A,B). The NE–SW-trending GP is also distributed

within the QDP, and it cuts the earlier QMP and the Cu orebody (Figure 2A). The QDP contains minor sulfides, such as chalcopyrite, pyrite, and molybdenite. Petrographic characteristics of the three types of porphyry intrusions are listed in Table 1 and shown in Figure 3.

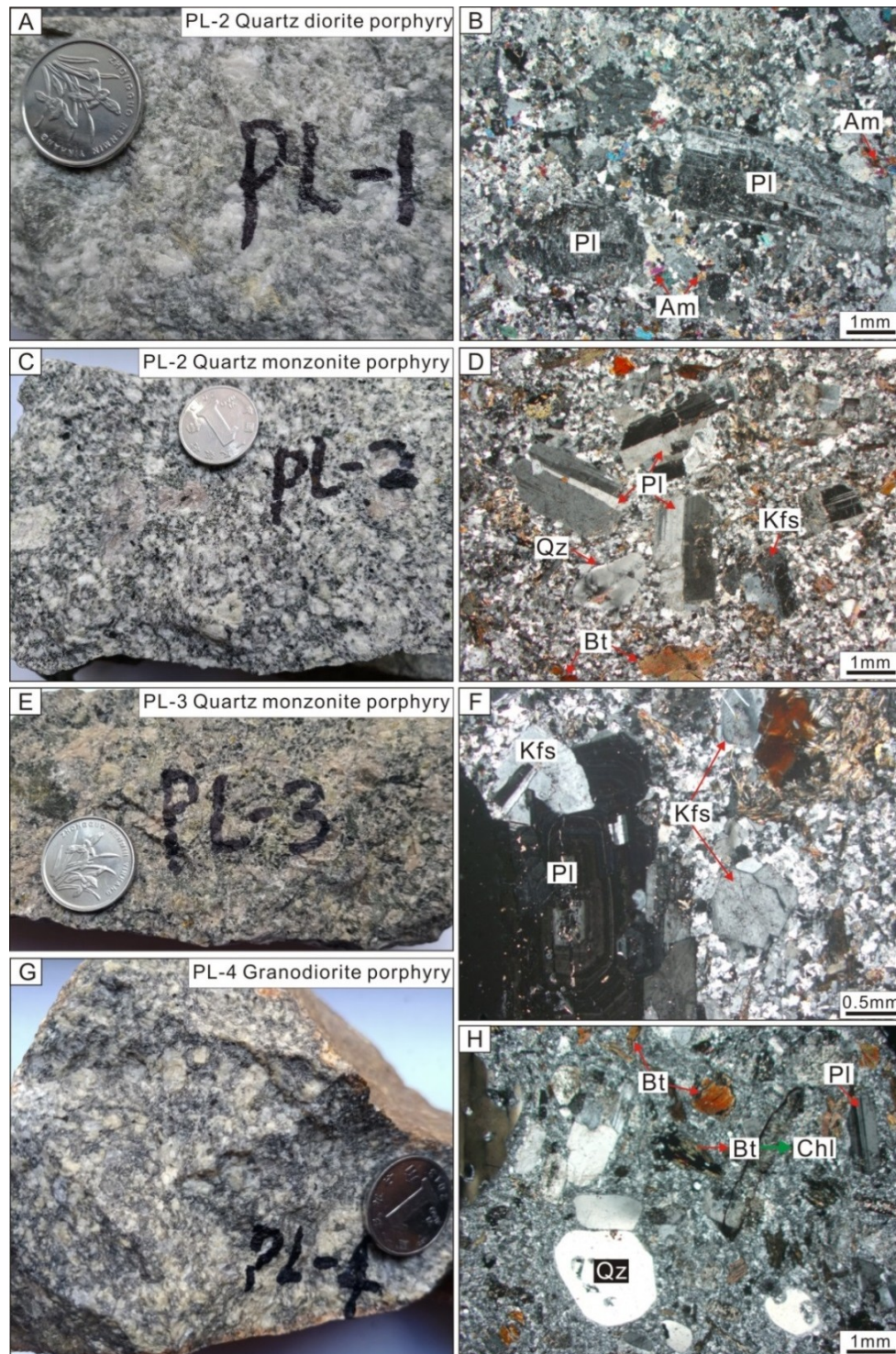


**Figure 3.** Hand specimen photographs and thin section photomicrographs of the porphyry intrusions in the Pulang ore district. (A,B) Quartz diorite porphyry (B under cross-polarized light). (C–F) Quartz monzonite porphyry (D and F under cross-polarized light). (G,H) Granodiorite porphyry (H under cross-polarized light). Abbreviations: Qz: quartz; Pl: Plagioclase; Kfs: K-feldspar; Bt: Biotite; Am: Amphibole; Chl: chlorite.

**Table 1.** Characteristics of the porphyry intrusions in the Pulang ore district.

Sample No.	Lithology	Location	Texture/Structure	Phenocrysts	Matrix
PL-1	Quartz diorite porphyry	N: 28°02'49" E: 99°58'51"	Porphyritic texture, massive structure	Phenocrysts account for 20% of the rock mass and consist of plagioclase (~15%, 0.5–3.2 mm), amphibole (~3%, 0.3–1.8 mm), and quartz (~2%, 0.4–2.3 mm).	Matrix is primarily a fine-grained texture and is dominated by plagioclase with minor amphibole, K-feldspar, and quartz.
PL-2	Quartz monzonite porphyry	N: 28°03'44" E: 99°59'19"	Porphyritic texture, massive structure	Phenocrysts account for 20% of the rock mass and consist of plagioclase (~9%, 0.6–3.8 mm), K-feldspar (~7%, 0.4–3.4 mm), quartz (~3%, 0.5–2.8 mm), and biotite (~1%, 0.2–1.6 mm).	Matrix shows a fine-grained texture and is composed of plagioclase and K-feldspar with minor quartz and biotite.
PL-3	Quartz monzonite porphyry	N: 28°02'54" E: 99°58'57"	Porphyritic texture, massive structure	Phenocrysts account for 20% of the rock mass and consist of plagioclase (~9%, 0.6–3.8 mm), K-feldspar (~7%, 0.4–3.4 mm), quartz (~3%, 0.5–2.8 mm), and biotite (~1%, 0.2–1.7 mm).	Matrix shows a fine-grained texture and is composed of plagioclase and K-feldspar with minor quartz and biotite.
PL-4	Granodiorite porphyry	N: 28°02'07" E: 99°58'18"	Porphyritic texture, massive structure	Phenocrysts account for 20% of the rock mass and consist of plagioclase (~8%, 0.4–2.3 mm), quartz (~5%, 0.5–2.6 mm), biotite (~3%, 0.3–1.4 mm), amphibole (~2%, 0.2–1.2 mm), and K-feldspar (~2%, 0.5–2.0 mm).	Matrix shows a fine-grained texture and is composed of plagioclase and quartz with minor biotite and amphibole.

Six Cu orebodies were explored in the initial mining area, and the "multi-nodal" KT1 that mainly occurs in the interior of the QMP is the largest orebody (Figure 2) controlled by the Heishuitang fault. It is about 1600 m in length and has a width of 360–600 m in the south and 120–300 m in the north. The thickness of this orebody varies from 52 m to 700 m [20]. The Cu grade varies from 0.20% to 3.74% with an average grade of 0.52% and a grade variation coefficient of 68.69%. From the center to the outer edge, the thickness of the orebody decreases, as does the grade of Cu and other associated metals (0.001% to 0.030% Mo, average 0.010%; 0.06 to 0.87 g/t Au, average 0.18 g/t; and 0.34 to 3.93 g/t Ag, average 1.27 g/t). Ore samples in the Pulang deposit display vein (Figure 4A), veinlet (Figure 4B), stockwork, disseminated, dense-disseminated (Figure 4C), and taxitic (Figure 4D) structures. The metallic minerals are dominated by chalcopyrite (Figure 4E), pyrite (Figure 4F–H), pyrrhotite, bornite, molybdenite (Figure 4I), and minor magnetite. Metal minerals display xenomorphic granular (Figure 4E), idiomorphic–hypidiomorphic granular (Figure 4F), filling metasomatic (Figure 4G), cataclastic (Figure 4G), and scaly textures (Figure 4I). The non-metallic minerals include quartz, plagioclase, K-feldspar, biotite, amphibole, chlorite, epidote, sericite, and calcite.

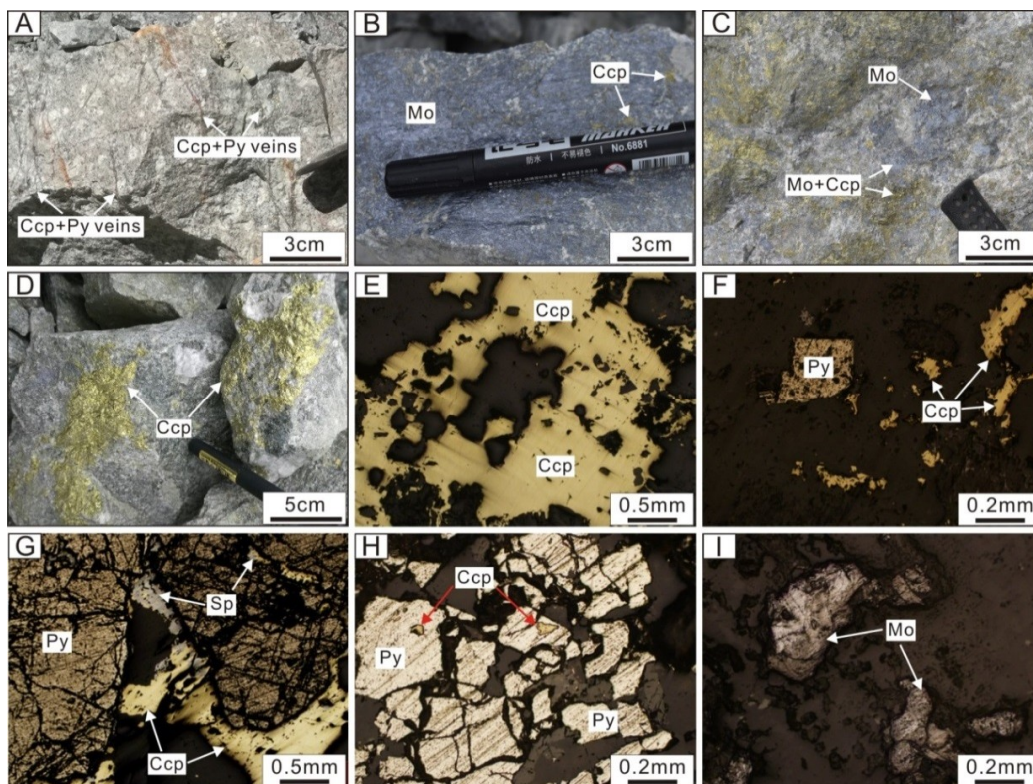


**Figure 4.** Photographs of ore fabrics and mineral assemblages of the Pulang porphyry Cu (–Mo–Au) deposit. (A) Chalcopyrite–pyrite veins and veinlets are distributed in the altered quartz monzonite porphyry. (B) Thin-film molybdenite veinlet. (C) Chalcopyrite intergrown with molybdenite that occurs as dense-disseminated in the altered quartz monzonite porphyry. (D) Nodular chalcopyrite. (E) Xenomorphic granular chalcopyrite. (F) Idiomorphic granular pyrite and xenomorphic granular chalcopyrite. (G) Chalcopyrite replaced by sphalerite, and they were filled into the fissures of pyrite. (H) Pyrite showing a cataclastic texture; and chalcopyrite filling into the holes of pyrite. (I) Scaly molybdenite. Abbreviations: Ccp: chalcopyrite; Py: pyrite; Mo: molybdenite; Sp: sphalerite.

The hydrothermal alteration in the Pulang deposit mainly includes silicification, K-feldspar alteration, sericitization, chloritization, epidotization, and carbonation. A typical porphyry alteration zoning occurs in this deposit from the center to the outer edge zone. An inner alteration zone is located at the core of the QMP and consists of extensive hydrothermal K-feldspar and quartz assemblages, which resulted from alteration of the plagioclase in the wall rock. Subsequently, the primary

K-feldspar, plagioclase, and biotite were altered to silicification and sericitization assemblages, with minor K-feldspathization forming the silicification–sericitization alteration zone, the latter of which is accompanied by economic Cu orebodies. The outer alteration zone (propylitization zone) is characterized by chloritization, epidotization with minor silicification, and carbonation.

On the basis of field research, cross-cutting relationships, mineral paragenetic associations, and associated hydrothermal alteration, the mineralization processes of the Pulang deposit can be divided into the following four stages: quartz + K-feldspar  $\pm$  pyrite veins (Stage I); quartz + molybdenite  $\pm$  chalcopyrite  $\pm$  pyrite veins (Stage II); quartz + chalcopyrite + pyrite  $\pm$  pyrrhotite  $\pm$  molybdenite veins (Stage III); and quartz + calcite  $\pm$  pyrite veins (Stage IV). Stage I is characterized by silicification and K-feldspathization with minor idiomorphic–hypidiomorphic disseminated pyrite mineralization distributed in the quartz–K-feldspar veins and host rocks. Stage II is characterized by the occurrence of molybdenite, with minor pyrite and chalcopyrite assemblages associated with silicification. The zone of Stage II silicification affected rocks that were slightly farther from the center of the orebody and around the margins of the zone of earlier K-feldspathization–silicification (Stage I). Stage III is the major Cu mineralization stage and is characterized by abundant precipitation of sulfide minerals accompanied by strong silicification and sericitization. Sulfides formed in this stage are dominated by chalcopyrite and pyrite (>85 vol.%), followed by bornite, pyrrhotite, and molybdenite. These sulfides generally replaced the earlier-formed pyrite and molybdenite, or filled in fractures of the earlier-formed euhedral pyrite (Figure 4G). The associated alteration including silicification and sericitization, as well as minor chloritization and epidotization, is distributed on both sides of the Stage III veins. Stage IV is the latest stage generating large numbers of quartz–calcite veins near the propylitization zone. Only minor disseminated pyrite was locally distributed in the veins and wall-rock. The abundant quartz and calcite minerals were observed in this stage.

## 4. Samples and Analytical Methods

### 4.1. LA-ICP-MS Zircon U–Pb Dating

Zircon grains were extracted from the quartz diorite porphyry, quartz monzonite porphyry, and granodiorite porphyry samples (Table 1) using magnetic and heavy liquid separation methods, and they were handpicked under a binocular microscope at the Integrity Geological Service Corporation in Langfang City, Heibei Province, China. The handpicked zircon grains were then mounted in epoxy resin and polished to expose crystal cores. All the zircon grains were examined under reflected and transmitted light with an optical microscope. Cathodoluminescence (CL) images, obtained using a JEOL scanning electron microscope (JEOL, Tokyo, Japan), were used to reveal their internal structures and to select spots for zircon U–Pb isotope analyses (Figure 5). These analysis spots were usually chosen near rims in areas with oscillatory CL response, which represents the final crystallization age of these intrusions.

Samples for LA-ICP-MS zircon U–Pb analyses were performed using a quadrupole ICP-MS (Agilent 7500c, Agilent Technologies, Santa Clara, CA, USA) coupled with an 193 nm ArF excimer laser (COMPexPro 102; Coherent, Santa Clara, CA, USA) equipped with an automatic positioning system, at the Key Laboratory of Mineral Resources Evaluation in Northeast Asia, Ministry of Natural Resources of China, Changchun, Jilin Province, China. The diameter of the laser spot was 32  $\mu$ m. A zircon standard (91500) and the National Institute of Science and Technology (NIST) 610 reference standard were analyzed after each set of six unknown analyses. The external zircon standard was used to correct for isotope ratio fractionation. The NIST610 reference standard was used in calculations of element concentrations and Si was used as an internal standard. Uncertainties on isotope ratios and ages are presented as  $\pm 2\sigma$ . The detailed analytical process and data reduction methodology are described in detail by Hou et al. [38], and the isotope data were calculated using the GLITTER (Version 4.0) [39]. Concordia diagram and weighted-mean age calculations were produced using ISOPLOT (Version 3.0) [40]. Common Pb was corrected following the method of Anderson [41].

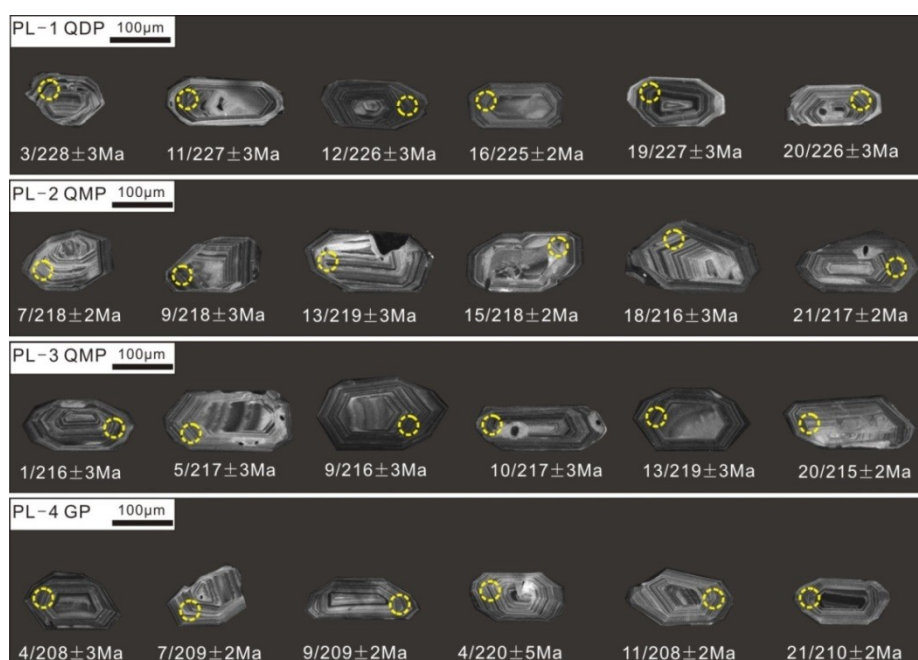


**Figure 5.** Cathodoluminescence (CL) images of respective zircon grains from the samples of Pulang porphyry intrusions. Yellow circles denote the locations of U–Pb dating. Abbreviations: QDP: Quartz diorite porphyry; QMP: Quartz monzonite porphyry; GP: Granodiorite porphyry.

#### 4.2. Molybdenite Re–Os Dating

Minor disseminated molybdenite in the Pulang deposit were recognized in the QDP, and most of the molybdenite occurred as vein and dense-disseminated in the QMP. Six molybdenite samples from different ore-hosting porphyry intrusions in the Pulang Cu (–Mo–Au) deposit, including three QMP-hosted and three QDP-hosted samples, were collected for Re–Os dating. Molybdenite grains were magnetically separated and handpicked using a binocular microscope (purity > 99%). The Re–Os isotope analyses were performed at the Re–Os Isotope Laboratory, National Research Center of Geoanalysis (NRCG), Chinese Academy of Geological Sciences (CAGS), Beijing, China. Samples were dissolved and equilibrated with  $^{185}\text{Re}$ - and  $^{190}\text{Os}$ -enriched spikes using alkaline fusion. The separation of rhenium from matrix elements was achieved by solvent extraction and cation exchange resin chromatography, while osmium was distilled as  $\text{OsO}_4$  from an  $\text{H}_2\text{SO}_4\text{--Ce}(\text{SO}_4)_2$  solution. The Re and Os concentrations as well as their isotopic compositions were made by an inductively coupled plasma mass spectrometer (TJA X-series ICP-MS, Thermo Fisher Scientific, Waltham, MA, USA). Detailed chemical procedure of Re–Os analytical methods used in this study can be followed by Shirey and Walker [42] and Du et al. [43]. The analytical reliability was tested by analyses of the JDC standard certified reference material GBW04436. Molybdenite model ages were calculated by  $t = [\ln(1 + ^{187}\text{Os}/^{187}\text{Re})]/\lambda$ , where  $\lambda$  is the decay constant of  $^{187}\text{Re}$ ,  $1.666 \times 10^{-11} \text{ year}^{-1}$  [44]. The Isoplot/Ex (Version 3.0) [40] was used for calculating the isochron age and drawing isochronological age diagrams. Absolute uncertainties of the Re–Os data are given at the  $2\sigma$  level.

#### 4.3. Major and Trace Element Concentrations

Following the removal of weathered surfaces, a total of 23 whole-rock samples were crushed and ground to ~200 mesh using an agate mill. Major and trace element compositions were analyzed by inductively coupled plasma optical emission spectroscopy (ICP-OES; Leeman Prodigy; precision better than  $\pm 1\%$ ) and inductively coupled plasma mass spectrometry (ICP-MS; Agilent–7500a; precision better than  $\pm 5\%$ ), respectively, at the Experiment Center, China University of Geosciences, Beijing, China.

## 5. Analytical Results

### 5.1. Zircon U–Pb Dating

Zircon U–Pb dating results of the quartz diorite porphyry (QDP, PL-1), and quartz monzonite porphyry (QMP, PL-2, PL-3) and granodiorite porphyry (GP, PL-4) in the Pulang deposit are listed in Table S1 and shown in Figure 6. All zircon grains from different types of porphyry samples are euhedral–subhedral in shape and transparent or pale brown in color, and exhibit marked oscillatory growth zoning in CL images (Figure 5). Most of them have high Th/U ratios (0.3–1.7; Table S1), indicating their magmatic origin [45–50]. For sample PL-1, the  $^{206}\text{Pb}/^{238}\text{U}$  ages from 23 analytical spots range from  $220 \pm 3$  Ma to  $233 \pm 3$  Ma, with a concordant U–Pb age of  $228 \pm 1$  Ma ( $2\sigma$ , MSWD = 0.30,  $N = 23$ ; Figure 6A) and a weighted mean age of  $227 \pm 2$  Ma ( $2\sigma$ , MSWD = 1.8,  $N = 23$ ; Figure 6A). The  $^{206}\text{Pb}/^{238}\text{U}$  ages of 21 analytical spots from sample PL-2 range from  $214 \pm 3$  Ma to  $225 \pm 4$  Ma, with concordant U–Pb and weighted mean ages of  $218 \pm 1$  Ma ( $2\sigma$ , MSWD = 0.43,  $N = 21$ ) and  $218 \pm 1$  Ma ( $2\sigma$ , MSWD = 0.78,  $N = 21$ ; Figure 6B), respectively. For sample PL-3, 21 analytical spots yield  $^{206}\text{Pb}/^{238}\text{U}$  ages ranging from  $215 \pm 2$  Ma to  $224 \pm 3$  Ma, which give a concordant U–Pb age of  $219 \pm 1$  Ma ( $2\sigma$ , MSWD = 0.25,  $N = 21$ ; Figure 6C) and a weighted mean age of  $219 \pm 1$  Ma ( $2\sigma$ , MSWD = 1.18,  $N = 21$ ; Figure 6C). Twenty-one analytical spots from the sample PL-4 yield  $^{206}\text{Pb}/^{238}\text{U}$  ages ranging from  $204 \pm 2$  Ma to  $211 \pm 3$  Ma, and yield a concordant U–Pb age of  $209 \pm 1$  Ma ( $2\sigma$ , MSWD = 0.33,  $N = 21$ ; Figure 6D) and a weighted mean age of  $209 \pm 1$  Ma ( $2\sigma$ , MSWD = 0.98,  $N = 21$ ; Figure 6D). These ages represent the emplacement ages of intrusions in the Pulang Cu (–Mo–Au) deposit.

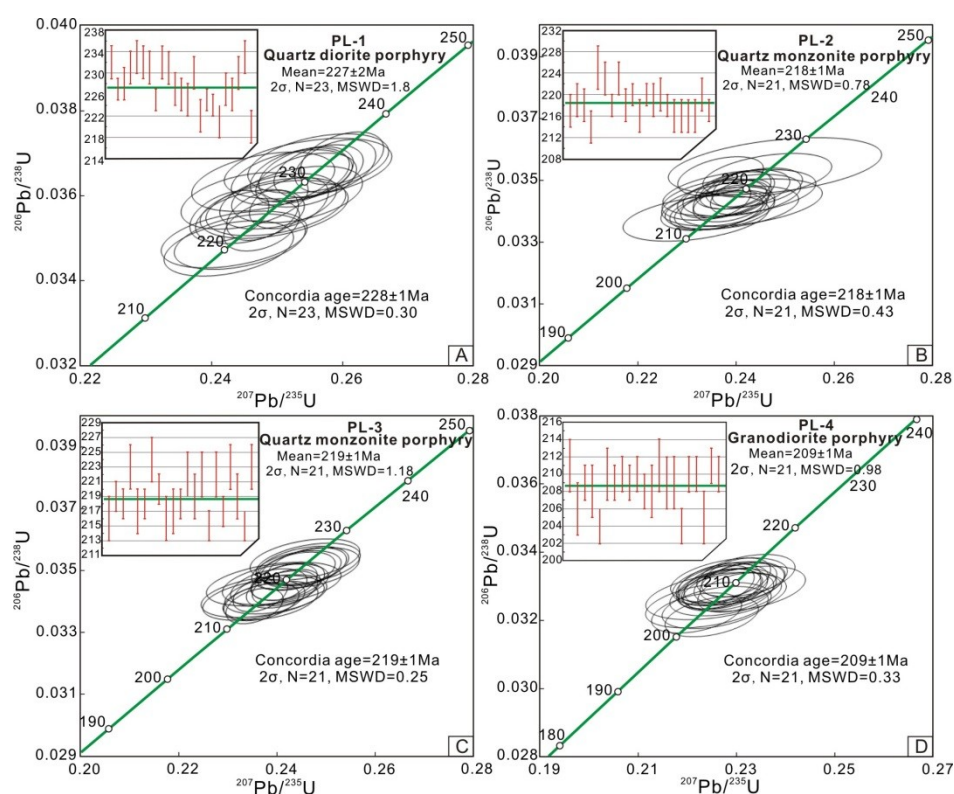


**Figure 6.** Zircon U–Pb concordia diagrams for samples of the quartz diorite porphyry (A), quartz monzonite porphyry (B,C), and granodiorite porphyry (D) in the Pulang Cu (–Mo–Au) deposit.

### 5.2. Molybdenite Re–Os Dating

The Re–Os isotopic compositions of six molybdenite samples obtained from the Pulang Cu deposit are presented in Table 2 and Figure 7. The Re and common Os concentrations are 101.22–933.39  $\mu\text{g/g}$

and 0.0164–0.5393 ng/g, respectively, and the  $^{187}\text{Re}$  and  $^{187}\text{Os}$  compositions are 63.62–586.65  $\mu\text{g/g}$  and 230.17–2129.61 ng/g, respectively. The six molybdenite samples yield a well-constrained Re–Os isochron age of  $218 \pm 2$  Ma ( $2\sigma$ , MSWD = 0.23, N = 6; Figure 7A), and a weighted average age of  $217 \pm 1$  Ma ( $2\sigma$ , MSWD = 0.23, N = 6; Figure 7B). The isochron age ( $218 \pm 2$  Ma) represents Cu mineralization age of the Pulang deposit.

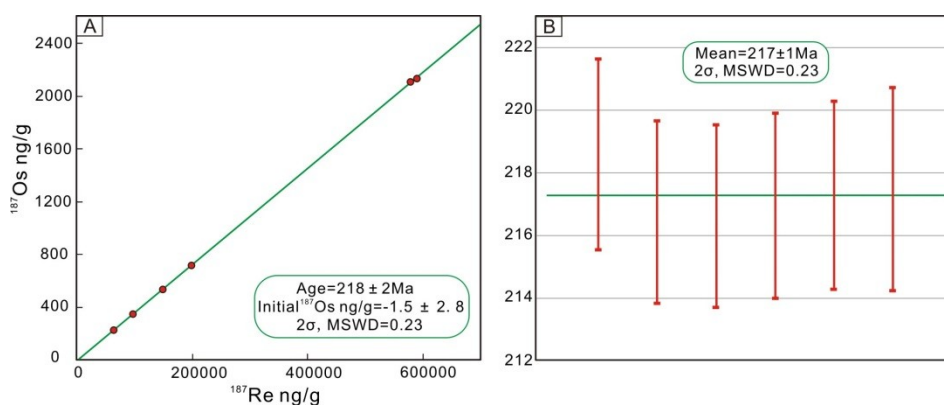


**Figure 7.** Diagrams of molybdenite Re–Os isochron age (A) and weighted mean age (B) in the Pulang Cu (–Mo–Au) deposit.

### 5.3. Major and Trace Element

The whole-rock major and trace elemental compositions for the QDP (PL-1), QMP (PL-2, PL-3), and GP (PL-4) in the Pulang deposit are listed in Table S2. Overall, the three different porphyry intrusions show wide-ranging compositional variation in terms of major elements. The QDP has an  $\text{SiO}_2$  content of 61.90–64.24 wt %, a  $\text{K}_2\text{O}$  content of 1.10–1.14 wt %, a  $\text{CaO}$  content of 5.05–6.18 wt %, and an  $\text{MgO}$  content of 3.26–4.19 wt %, with  $\text{Mg\#}$  [ $\text{Mg\#} = 100 \times \text{Mg}^{2+} / (\text{Mg}^{2+} + \text{TFe}^{2+})$ ] values varying from 68 to 73. Compared with the QDP, the QMP and GP have higher  $\text{SiO}_2$  (QMP = 64.32–67.69 wt %, GP = 69.95–74.10 wt %) and  $\text{K}_2\text{O}$  (QMP = 2.53–4.33 wt %, GP = 2.0–3.01 wt %), but relatively lower  $\text{CaO}$  (QMP = 2.60–3.85 wt %, GP = 1.49–2.14 wt %) and  $\text{MgO}$  (QMP = 1.69–2.06 wt %, GP = 1.80–3.23 wt %), with  $\text{Mg\#}$  value (QMP = 46–60, GP = 47–71). In addition, the  $\text{Al}_2\text{O}_3$  content of the GP (11.39–12.11 wt %) is lower than that of QDP (15.43–16.17 wt %) and QMP (14.32–16.07 wt %). The  $\text{TiO}_2$ ,  $\text{Fe}_2\text{O}_3\text{T}$ ,  $\text{Na}_2\text{O}$ ,  $\text{P}_2\text{O}_5$ , and aluminum saturation index (A/CNK) of the three porphyry intrusions are similar, ranging from 0.40 to 0.77 wt %, from 2.17 to 4.56 wt %, from 2.46 to 4.98 wt %, from 0.23 to 0.45 wt %, and from 0.77 to 1.08, respectively. For  $\text{SiO}_2$  vs.  $\text{K}_2\text{O} + \text{Na}_2\text{O}$  diagram (Figure 8A [51]), data for all samples are plotted within fields of the subalkaline series. In the  $\text{SiO}_2$  vs.  $\text{K}_2\text{O}$  (Figure 8B [52]) and  $\text{Na}_2\text{O}$  vs.  $\text{K}_2\text{O}$  diagrams (Figure 8C [53]), data for QDP samples are plotted within fields of the middle-K calc-alkaline series and sodic suites, whereas data for the QMP and GP samples are plotted within fields of the high-K calc-alkaline series and potassic suites (Figure 8B,C). All samples have a narrow range of A/CNK (mole [ $\text{Al}_2\text{O}_3 / (\text{CaO} + \text{Na}_2\text{O} + \text{K}_2\text{O})$ ]) ratio values (A/CNK = 0.77–1.08), indicating metaluminous to moderately peraluminous in an A/NK vs. A/CNK diagram (Figure 8D [54]).

In the chondrite-normalized REE diagram (Figure 9A), the three different petrographic porphyry intrusions are depleted of heavy rare-earth elements (HREEs) relative to light rare-earth elements (LREEs), with slightly negligible Eu anomalies ( $\text{Eu}/\text{Eu}^* = 0.79\text{--}0.97$ ). The QMP [ $(\text{La}/\text{Yb})_{\text{N}} = 17.0\text{--}25.9$ ] are more fractionated than the GP [ $(\text{La}/\text{Yb})_{\text{N}} = 9.3\text{--}16.8$ ] and QDP [ $(\text{La}/\text{Yb})_{\text{N}} = 7.6\text{--}9.0$ ]. In the MORB-normalized geochemical pattern (Figure 9B), they display similar REE patterns, and all are characterized by a depletion of high field-strength elements (HFSEs; e.g., Nb, Ta, and Ti). They are characterized by high Sr (432–1150 ppm), and low Y (9–16 ppm) and Yb (0.8–1.5 ppm) concentrations, with high Sr/Y ratios (48–94).

**Table 2.** Molybdenite Re–Os dating results in the Pulang Cu (–Mo–Au) deposit.

Sample No.	Lithology	Ore-Hosted Rocks	Location	Re ( $\mu\text{g/g}$ )		Common Os (ng/g)		$^{187}\text{Re}$ ( $\mu\text{g/g}$ )		$^{187}\text{Os}$ (ng/g)		Model Age (Ma)	
				Measured	Error	Measured	Error	Measured	Error	Measured	Error	Measured	Error
PL-8-6	Mo-bearing quartz veinlet ore	QDP	N: 28°02'45" E: 99°58'53"	921.25	8.08	0.0184	0.4222	579.03	5.08	2112.44	13.19	218.6	3.0
PL-11-2	Disseminated Mo-bearing chalcopyrite ore	QMP	N: 28°02'53" E: 99°59'04"	101.22	0.65	0.2262	0.4283	63.62	0.41	230.17	1.42	216.8	2.9
PL-11-3	Disseminated Mo-bearing chalcopyrite ore	QMP	N: 28°02'53" E: 99°59'04"	154.64	1.01	0.0164	0.3759	97.19	0.64	351.44	2.09	216.6	2.9
PL-10-4	Mo-bearing quartz veinlet ore	QDP	N: 28°02'56" E: 99°58'52"	316.48	2.15	0.4501	0.4819	198.91	1.35	720.58	4.47	217.0	2.9
PL-11-5	Mo-bearing chalcopyrite quartz vein ore	QDP	N: 28°02'53" E: 99°59'26"	236.07	1.64	0.5393	0.2190	148.37	1.03	538.16	3.42	217.3	3.0
PL-7-1	Mo-bearing quartz lump ore	QMP	N: 28°02'49" E: 99°59'10"	933.39	8.19	0.0187	0.4278	586.65	5.15	2129.61	13.64	217.5	3.2

Note: QDP: Quartz diorite porphyry; QMP: Quartz monzonite porphyry.

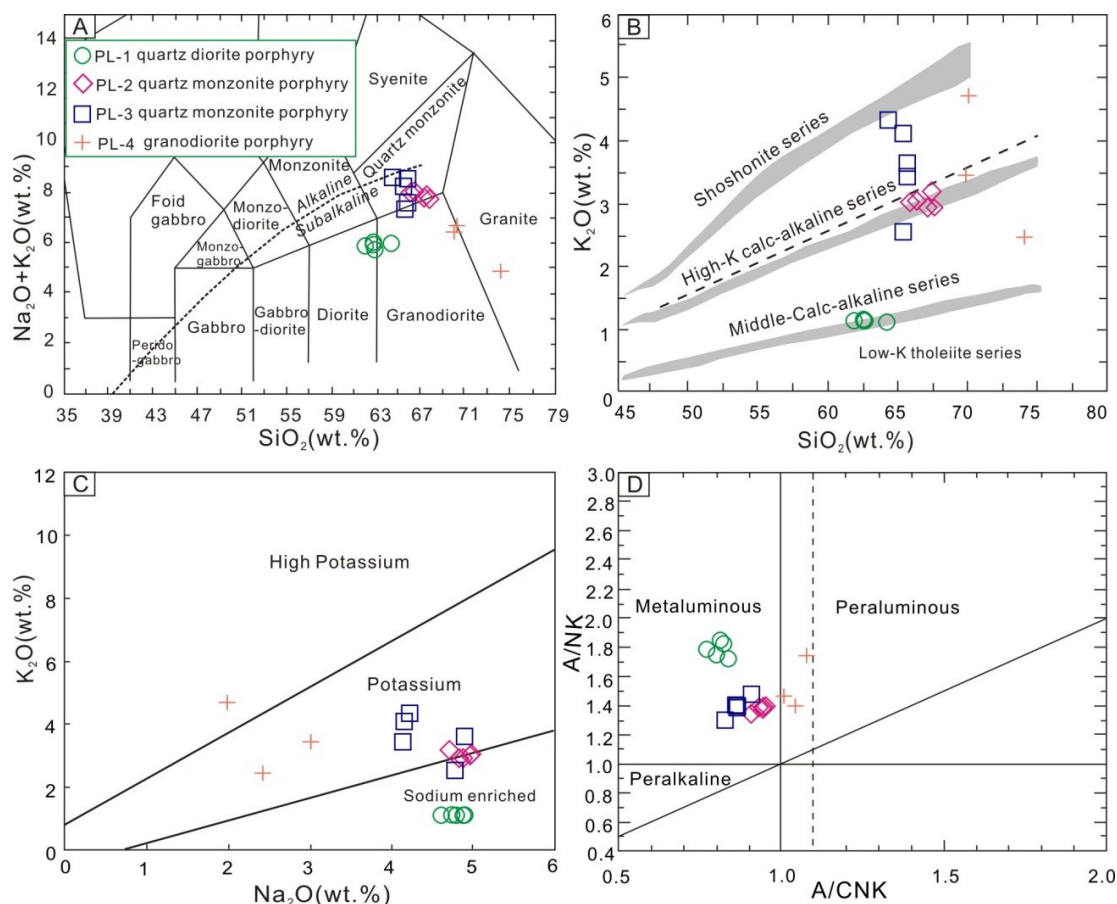


**Figure 8.** (A) Diagrams of  $\text{SiO}_2$  vs.  $\text{Na}_2\text{O} + \text{K}_2\text{O}$  (based on Irvine and Baragar [51]); (B)  $\text{SiO}_2$  vs.  $\text{K}_2\text{O}$  (based on Peccerillo and Taylor [52]); (C)  $\text{Na}_2\text{O}$  vs.  $\text{K}_2\text{O}$  (based on Middlemost [53]); (D)  $\text{A}/\text{CNK}$  vs.  $\text{A}/\text{NK}$  for the Pulang porphyry intrusions (based on Maniar and Piccoli [54]).

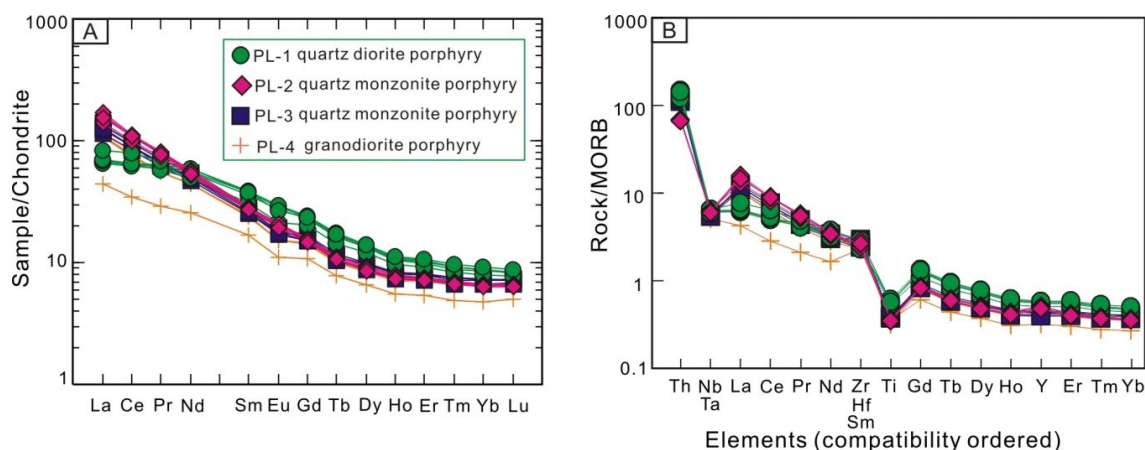


**Figure 9.** (A) Chondrite-normalized REE patterns and (B) MORB-normalized geochemical patterns for the Pulang porphyry intrusions (based on Pearce [55]). Chondrite and N-MORB values are from Boynton [56] and Sun and McDiough [57], respectively.

## 6. Discussion

### 6.1. Timing of Magmatism and Cu Mineralization

Some previous geochronological studies on the QDP, QMP, and GP in Pulang obtained a coeval age. For example, Wang et al. [14] obtained LA-ICP-MS zircon U–Pb ages of  $214 \pm 3$  Ma,  $214 \pm 3$  Ma,

and  $209 \pm 4$  Ma for QDP, QMP, and GP, respectively; Wang et al. [22] obtained SHRIMP zircon U–Pb ages of  $228 \pm 3$  Ma and  $226 \pm 3$  Ma for QDP and QMP, respectively. These isotope dating results have led to the conclusion that all the QDP, QMP, and GP contribute to the Pulang Cu mineralization. However, the ages of QDP ( $228 \pm 3$  Ma) and QMP ( $226 \pm 3$  Ma) are incompatible with the reported molybdenite Re–Os isochron ages ( $208 \pm 15$  Ma and  $213 \pm 4$  Ma [3,18,24]). In this study, the U–Pb concordia age of the zircon coincides well with the weighted mean  $^{206}\text{Pb}/^{238}\text{U}$  age in every porphyry intrusion sample (Figure 6), suggesting more accurate and reliable dating. Our new dating results for QMP ( $218 \pm 1$  Ma and  $219 \pm 1$  Ma) show that it is younger than QDP ( $227 \pm 2$  Ma) by about 9 Ma, and it is older than GP ( $209 \pm 1$  Ma) by about 10 Ma, indicating that the three different porphyry intrusions were not formed coevally. This conclusion is further supported by the geological fact that the QMP and GP display as small dykes intruding into the QDP (Figure 2), and that the GP cuts both QMP and orebodies (Figure 2). The Pulang porphyry intrusions were not formed coevally, which makes it unlikely that the Pulang porphyry intrusions all contributed to Cu mineralization. To constrain the mineralization age accurately, we performed the molybdenite Re–Os dating, and the result is that the six molybdenite-bearing samples from the Pulang deposit yielded a well-constrained isochron age of  $218 \pm 2$  Ma, and a weighted mean age of  $217 \pm 1$  Ma (Figure 7). The precise zircon U–Pb and Re–Os ages indicate a close temporal relationship between Cu mineralization and QMP. In addition, Cu mineralization in the Pulang deposit mainly occurred within the QMP (Figure 7), and only minor mineralization developed in the QDP. From the center (QMP) to the outer edge (QDP), the thickness of the orebody decreases, as does the grade of Cu and other associated metals (0.030–0.001% Mo, average 0.010%; 0.87–0.06g/t Au, average 0.18 g/t; and 3.93–0.34 g/t Ag, average 1.27 g/t), which also suggests a spatial relationship between Cu mineralization and QMP. Moreover, the Pb isotope compositions of sulfur minerals ( $^{206}\text{Pb}/^{204}\text{Pb} = 18.079\text{--}18.694$ ,  $^{207}\text{Pb}/^{204}\text{Pb} = 15.603\text{--}15.632$ , and  $^{208}\text{Pb}/^{204}\text{Pb} = 38.228\text{--}38.635$  [58]) in Pulang are similar and homogeneous, and they coincide well with those of the QMP ( $^{206}\text{Pb}/^{204}\text{Pb} = 18.3005\text{--}18.5431$ ,  $^{207}\text{Pb}/^{204}\text{Pb} = 15.6061\text{--}15.6318$  and  $^{208}\text{Pb}/^{204}\text{Pb} = 38.4352\text{--}38.856$  [58]), but significantly differ from those of the QDP ( $^{206}\text{Pb}/^{204}\text{Pb} = 18.8761\text{--}19.1700$ ,  $^{207}\text{Pb}/^{204}\text{Pb} = 15.6191\text{--}15.6413$ , and  $^{208}\text{Pb}/^{204}\text{Pb} = 39.3458\text{--}39.5706$  [23]). Furthermore, the Cu concentrations (Table S2) of QMP range from 343 to 5220 ppm (average = 1989 ppm), largely exceeding the Cu concentrations in QDP (113–117 ppm, average = 115 ppm) and GP (222–229 ppm, average = 225 ppm); this finding indicates that ore-forming materials in the Pulang deposit were mainly sourced from QMP. To summarize, geological, geochronological, isotopic, and geochemical data led to the conclusion that Cu mineralization in Pulang was spatially, temporally, and genetically related to the QMP rather than the QDP and GP.

The zircon U–Pb ages of QMP ( $218 \pm 1$  Ma and  $219 \pm 1$  Ma) are consistent with molybdenite Re–Os age ( $218 \pm 2$  Ma), constraining the timing of emplacement and associated Cu mineralization in the Pulang Cu (–Mo–Au) deposit to the Late Triassic (~217 Ma). Moreover, these ages are broadly consistent with the zircon U–Pb and mineralization ages of some porphyry-type Cu deposits located in the same metallogenic belt of the southern Yidun Arc, such as Xuejiping, Lannitang, Songnuo, and Chundu (Table 3). Thus, the zircon U–Pb and Re–Os isochron ages, reported herein and previously, constrain the Late Triassic magmatism and associated Cu mineralization event to the southern Yidun Arc.

**Table 3.** Geological characteristics of the major Late Triassic Cu deposits in the southern Yidun Arc.

Deposit	Type	Commodity	Reserve/Grade	Ore-Hosting Rock	Metal Minerals	Alteration	Related Intrusion Age (Ma)	Mineralization Age (Ma)	Reference
Pulang	Porphyry	Cu–Mo–Au	Cu: 1.14 Mt @ 0.52% Mo: 6399 t @ 0.0004% Au: 54 t @ 0.18 g/t	QDP, QMP, GP	Ccp, Py, Mo, Bn, Mag, Sp, Pyr, Cv	Qz, Kfs, Ser, Chl, Ep, Cal	QMP (Zircon U–Pb: 218 ± 1, 219 ± 1)	Molybdenite Re–Os: 219 ± 2	This paper [20]
Xuejiping	Porphyry	Cu	Cu: 0.30 Mt @ 0.52%	DP, QMP	Ccp, Py, Mo, Gn, Sp	Qz, Kfs, Ser, Chl, Ep, Cal	QMP (Zircon U–Pb: 219 ± 2, 215 ± 3)	Molybdenite Re–Os 221 ± 2	[7,55]
Chundu	Porphyry	Cu	No data	DP, QMP, GP	Ccp, Py, Gn, Sp	Qz, Kfs, Ser, Chl, Ep, Cal	QMP (Zircon U–Pb: 220 ± 2)	Triassic	[2]
Lannitang	Porphyry	Cu	Cu: 0.18 Mt @ 0.5%	QDP, QMP	Ccp, Py, Clc, Mag, Hem	Qz, Kfs, Chl, Ep	QDP (Zircon U–Pb: 225 ± 4)	Triassic	[33]
Songnuo	Porphyry	Cu	No data	QMP	Ccp, Py, Pyr	Qz, Chl, Ep, Cal	QMP (Zircon U–Pb: 221 ± 4)	Triassic	[9]
Langdu	Skarn	Cu–Fe	Cu: 0.10 Mt @ 6%	Skarn and hornfel	Ccp, Py, Pyr, Mag	Qz, Grt, Tr, Chl, Ep, Cal	QMP (Zircon U–Pb: 223 ± 1)	Triassic	[33]

Abbreviations: QDP: quartz diorite porphyry; QMP: quartz monzonite porphyry; GP: granodiorite porphyry; DP: diorite porphyry; Ccp: chalcocopyrite; Py: pyrite; Mo: molybdenite; Bn: bornite; Mag: magnetite; Sp: sphalerite; Gn: galena; Pyr: pyrrhotite; Clc: chalcocite; Cv: covellite; Hem: hematite; Qz: quartz; Kfs: K-feldspar; Ser: sericite; Chl: chlorite; Grt: garnet; Tr: tremolite; Ep: epidote; Cal: calcite.

## 6.2. Petrogenesis and Tectonic Setting

A large number of geochronological data indicate that Late Triassic magmatism in the Yidun Arc lasted for at least 29 Ma from ~235 to ~206 Ma with a peak age at around 215 Ma [59–61]. According to the sequence of magma intrusion for the Pulang porphyry intrusions, it is clear that the SiO<sub>2</sub> content of the rocks increases gradually from QDP to QMP and then to GP, which indicates that the Late Triassic Pulang porphyry intrusions are the products of different evolution stages of the same magmatism in the same tectonic setting.

Pulang porphyry intrusions have high SiO<sub>2</sub> (62–74 wt %), Al<sub>2</sub>O<sub>3</sub> (11.4–16.2 wt %, mostly >15.0 wt %), Na<sub>2</sub>O (2.4–5.0 wt %, mostly >4.0 wt %), Sr (432–1150 ppm), Mg# values (46–73), and Sr/Y ratios (48–94), and they have low Y (9–16 ppm) and Yb values (0.8–1.5 ppm), as well as moderately negative Eu anomalies (Eu/Eu\* = 0.79–0.97), suggesting a geochemical affinity to adakitic rocks [62–65]. In the (La/Yb)<sub>N</sub> vs. Yb<sub>N</sub> and Sr/Y vs. Y geochemical classification diagrams (Figure 10A,B), most samples of the Pulang porphyry intrusions are plotted in the adakitic rocks field, and only a few samples are plotted in the transitional field between typical adakitic rocks and normal island arc rocks. Adakite was initially named for rocks with clear contributions from the partial melting of subducted young hot oceanic crust represented by mid-ocean ridge basalt (MORB) [62]. Some important geochemical characteristics of the adakites, such as high Sr and low Y and Yb, can be attributed to the presence of garnet ± amphibole and the absence of plagioclase within the melt residue [62,66–70]. To date, several genetic models have been proposed to explain the genesis of adakites, including (1) the assimilation of crustal material by a mantle-derived magma, and subsequent fractional crystallization (AFC model [64,71]), (2) the partial melting of the delaminated lower continental crust [72,73], (3) the partial melting of the thickened continental crust [74,75], and (4) the partial melting of a subducted oceanic slab [62–64].

To begin with, the fractionation of amphibole would result in high Sr/Y ratios, but there are no evident correlations between Sr/Y and SiO<sub>2</sub> (Figure 11A). The moderately negative Eu anomalies indicate little or no plagioclase fractionation. Fractional crystallization of a garnet-bearing assemblage from basaltic melts would result in a positive correlation between Sr/Y, La/Yb, and especially Dy/Yb ratios with increasing SiO<sub>2</sub> [10]. The Pulang porphyry intrusions do not show such correlation (Figure 11B). Instead, they display the clearly partial melting trends observed in the La/Yb vs. La and Rb/Nb vs. Rb diagrams (Figure 11C,D), indicating that the partial melting of the source plays a dominant role in the formation of the Pulang adakitic magmas. Moreover, adakitic magmas derived from the partial melting of thickened continental lower crust are characteristic of K-rich and low MgO magmas with low Mg# values (generally Mg# < 46) [66,71], which are not compatible with the geochemical features of the Pulang porphyry intrusions as described above. Moreover, adakitic magmas produced by the partial melting of delaminated lower crust generally have high MgO, Cr, Co, and Ni contents, which are similar to those of the Pulang porphyry intrusions. However, extensive isotope, geochemical, and geochronological data indicate that the delamination of the lower crust is inconsistent with the geological background of the Yidun Arc during the Late Triassic [10,14,33]. Finally, the geochemical characteristics of the Pulang adakitic porphyry intrusions and adakite are compared in detail (Table 4), and the comparison results indicate that Pulang adakitic porphyry intrusions are similar to adakite. Moreover, Pulang porphyry intrusions also have low TiO<sub>2</sub> (0.4–0.8 wt %), MgO (1.7–4.2 wt %), and CaO + Na<sub>2</sub>O (4.6–10.9 wt %) contents and low Cr/Ni ratios (1.2–7.6, mostly 1.2–3.9). As shown in the detailed geochemical comparison in Table 4, Pulang porphyry intrusions can be classified as high silica adakites (HSA) [63]. In the discrimination diagrams of Martin et al. (2005) [63], Pulang porphyry intrusion samples are plotted in the fields of HSA (Figure 10C–F). It is generally believed that HSA are derived from oceanic-slab melts that may react with mantle wedges during the ascent [62–65]. Together with the isotopic geochronology and the tectonic setting discussed below, we propose that Pulang HSA porphyry intrusions were derived from the partial melting of the subducted Ganzi-Litang oceanic plate that reacted with peridotite during its ascent through the mantle wedge. Their high-Mg# features are caused by the interaction between slab melts and mantle peridotite [76,77].

It is generally accepted that the formation of the Yidun Arc can be attributed to the westward subduction of the Ganzi–Litang oceanic lithosphere during the Late Triassic period, and that magmatic activity in the Yidun Arc lasted for at least 29 Ma, from ~235 to ~206 Ma [59–61]. The initial westward subduction of the Ganzi–Litang oceanic lithosphere began at ~235 Ma (following the earlier closure of the Jinshajiang Ocean), and finally ended at ~206 Ma, accompanied by the occurrence of syn-collision granites. The Late Triassic volcanic and intrusive rocks in the Yidun Arc are characterized by middle- to high-K calc-alkaline rock series with an I-type affinity [10,11,14], together with enrichment in LILEs and LREEs, and depletion of HFSEs and HREEs. These geochemical characteristics are similar to those of QDP, QMP, and GP in Pulang, indicating an island arc setting [78]. Moreover, in the Rb vs. Y + Nb, Rb vs. Yb + Ta, Nb vs. Y, and Rb/10 vs. Hf vs. Ta  $\times$  3 diagrams (Figure 12A–D), all the QDP, QMP and GP samples from Pulang are plotted within the volcanic arc granite (VAG) field, also consistent with a subduction-related volcanic arc setting. In the Th/Yb vs. Ba/La and Ba/Th vs. Th/Nb diagrams (Figure 12E,F), the Pulang samples show a trend similar to that of the melt-related enrichment rather than the fluid-related enrichment, indicating a source associated with subducted plate melting. This further supports the conclusion discussed above that Pulang adakitic porphyry intrusions are related to oceanic-slab-derived melts. Importantly, these geochemical characteristics at the Pulang Cu deposit are similar to those of the porphyry intrusions associated with Cu mineralization at the Xuejiping, Chundu, Lannitang, Songnuo, and Langdu Cu deposits in the southern Yidun Arc. Combining similar geochemical characteristics with similar mineralization ages and geological characteristics of these porphyry-type Cu deposits in the southern Yidun Arc (Table 3), we conclude that all of these Cu deposits can be attributed to the Late Triassic tectonic–magmatic–hydrothermal event that was induced by the westward subduction of the Ganzi–Litang oceanic lithosphere.

**Table 4.** Comparisons of geochemical characteristics between the adakite, high-SiO<sub>2</sub> adakites (HSA), low-SiO<sub>2</sub> adakites (LSA), and Pulang porphyry intrusions.

	Adakite	HSA	LSA	Pulang Porphyry Intrusions
SiO <sub>2</sub>	≥56 wt %	≥60 wt %	≤60 wt %	62–74 wt %
Al <sub>2</sub> O <sub>3</sub>	≥15 wt % (rarely lower)			11.4–16.2 wt % (mostly 15.1–16.2 wt %)
MgO	<3 wt % (rarely >6 wt %)	0.5–4.0 wt %	4.0–9.0 wt %	1.7–4.2 wt %
Na <sub>2</sub> O	3.5–7.5 wt %			2.7–5.0 wt % (mostly 3.4–5.0 wt %)
K <sub>2</sub> O/Na <sub>2</sub> O	~0.42 (sodic)			0.2–1.0 wt % (sodic)
CaO + Na <sub>2</sub> O		<11 wt %	>10 wt %	4.6–10.9 wt %
TiO <sub>2</sub>		<0.9 wt %	>3.0 wt %	0.40–0.77 wt %
Sr	>400 ppm (rarely <400 ppm)	<1100 ppm	>1000 ppm	432–1150 ppm
Y	≤18 ppm	≤18 ppm	≤18 ppm	9–16 ppm
Yb	≤1.9 ppm	≤1.9 ppm	≤1.9 ppm	0.8–1.5 ppm
Sr/Y	40–100			48–94
Cr/Ni		0.5–4.5	1.0–2.5	1.2–7.6 (mostly 1.2–3.9 wt %)
Mg#	~50			46–73 (>46, High-Mg)
Reference	[62,65]	[79]	[79]	This paper

Note: HSA: High-SiO<sub>2</sub> adakites; LSA: Low-SiO<sub>2</sub> adakites.

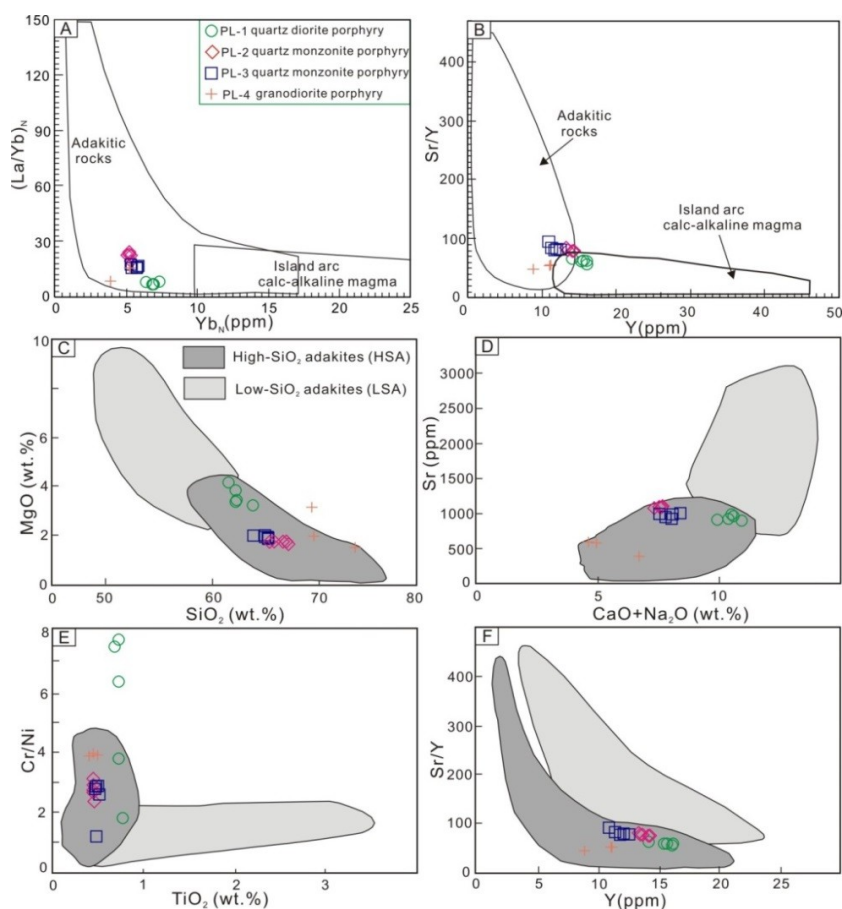


**Figure 10.** (A)  $(La/Yb)_N$  vs.  $(Yb)_N$  (based on Martin [79]), (B)  $Sr/Y$  vs.  $Y$  (Defant and Drummond [62]), (C)  $SiO_2$  vs.  $MgO$  (based on Martin et al. [63]), (D)  $SiO_2$  vs.  $Sr$  (based on Martin et al. [63]), (E)  $SiO_2$  vs.  $Cr/Ni$  (based on Martin et al. [63]), and (F)  $SiO_2$  vs.  $Sr/Y$  (based on Martin et al. [63]) discrimination diagrams for Pulang porphyry intrusions.

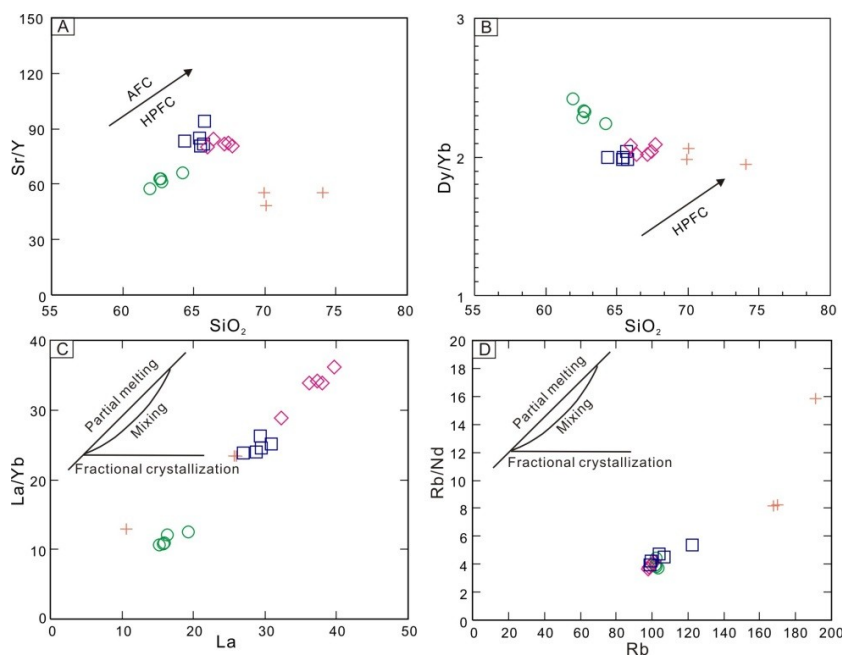


**Figure 11.** (A)  $Sr/Y$  vs.  $SiO_2$ , (B)  $Dy/Yb$  vs.  $SiO_2$ , (C)  $La/Yb$  vs.  $La$ , and (D)  $Rb/Nd$  vs.  $Rb$  diagrams for the Pulang porphyry intrusions. Symbols are as in Figure 10.

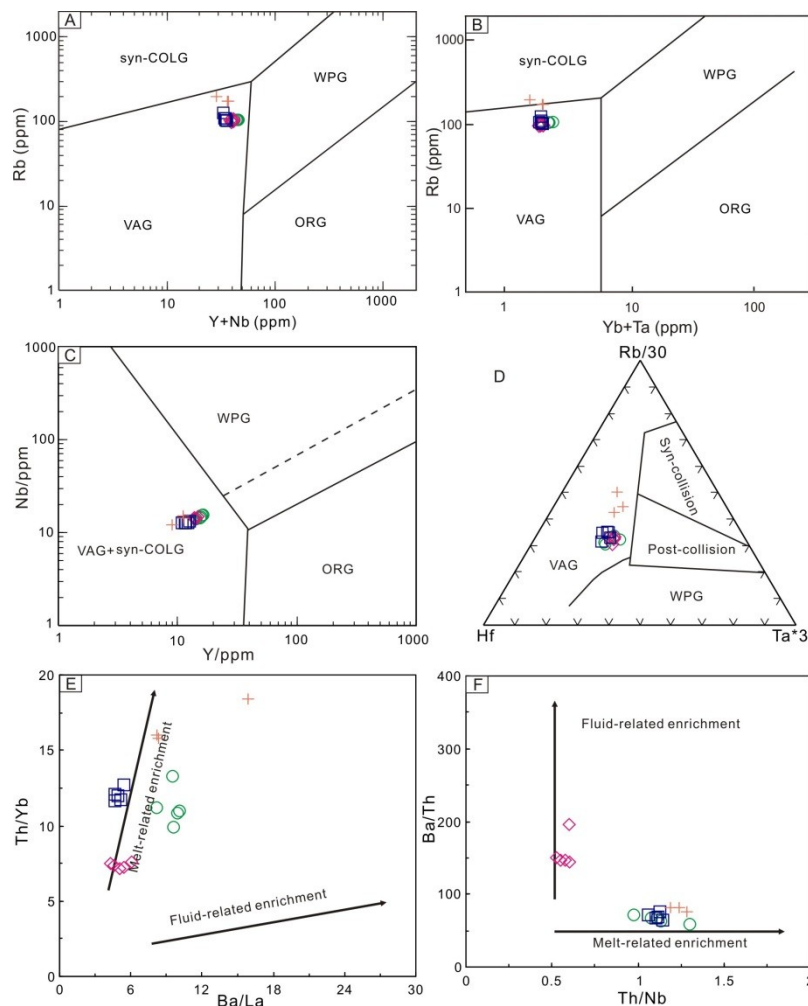


**Figure 12.** (A) Rb vs. Y + Nb (based on Pearce et al. [80]), (B) Rb vs. Yb + Ta (based on Pearce et al. [80]), (C) Y vs. Nb (based on Pearce [81]), and (D) Rb/30-Hf-Ta  $\times$  3 (based on Harris et al. [82]) tectonic discrimination diagrams for Pulang porphyry intrusions. (E) Th/Yb vs. Ba/La and (F) Ba/Th vs. Th/Nb diagrams showing the roles of the fluid- and melt-related enrichments of the source. Symbols are as in Figure 10.

### 6.3. Implications for the Cu Mineralization

The Yidun arc was formed during the Late Triassic in response to the westward subduction of the Ganzi–Litang oceanic plate. The Late Triassic bimodal volcanic suites and associated VMS-type deposits developed in the northern Yidun Arc, which can be attributed to a steep subduction. In contrast, the flat subduction in the southern Yidun Arc produced abundant adakitic porphyry intrusions and associated porphyry-type Cu deposits. This flat subduction is the most favorable tectonic setting for slab melting [83,84]. It has been recently proposed that oceanic-slab-derived adakites are genetically related to porphyry-type Cu–Au deposits [83–91]. Oceanic-slab-derived melts are considered to have high oxygen fugacity and high Cu concentrations to form adakitic magmas that may potentially produce porphyry Cu deposit [83–85]. At an oxygen fugacity above FMQ + 2 (FMQ refers to fayalite–magnetite–quartz oxygen buffer), sulfur and chalcophile elements (Cu, Au, etc.) easily form oxidized ionic compounds ( $\text{SO}_4^{2-}$ ) that cause the Cu to remain in magmas in the form of sulfate during the magma ascent. By contrast, at an oxygen fugacity below FMQ, sulfur presents mainly in its reduced form ( $\text{S}^{2-}$ ), which is less soluble in magmas. This leads to a premature precipitation of metallic elements in the mantle or deep crust, which is not good for the formation of porphyry Cu deposit [83]. For the Pulang deposit, the QMP associated with Cu mineralization

has a high oxygen fugacity ( $f_{O_2} > FMQ + 5.5$ ), and even the QDP of the barren mineralization has a high oxygen fugacity ( $f_{O_2} > FMQ + 5.1$ ) [14], indicating that the Pulang Cu deposit formed in a high oxygen fugacity environment. For another, Cu concentrations in the oceanic crust range from 60 to 130 ppm [92], which is much higher than those of the primitive mantle (30 ppm [93]) and the continental crust (27 ppm [84]). Therefore, basaltic oceanic-slab-derived melts (oceanic-slab-derived adakites) have considerably higher Cu content than the lower continental crust melt or mantle-derived melt [83], which is supported by the higher Cu concentrations for the QDP (113–117 ppm), QMP (343–5220 ppm), and GP (222–229 ppm) in Pulang. The combination of these factors contributed to the formation of the subduction-related Pulang porphyry deposit (Figure 13).

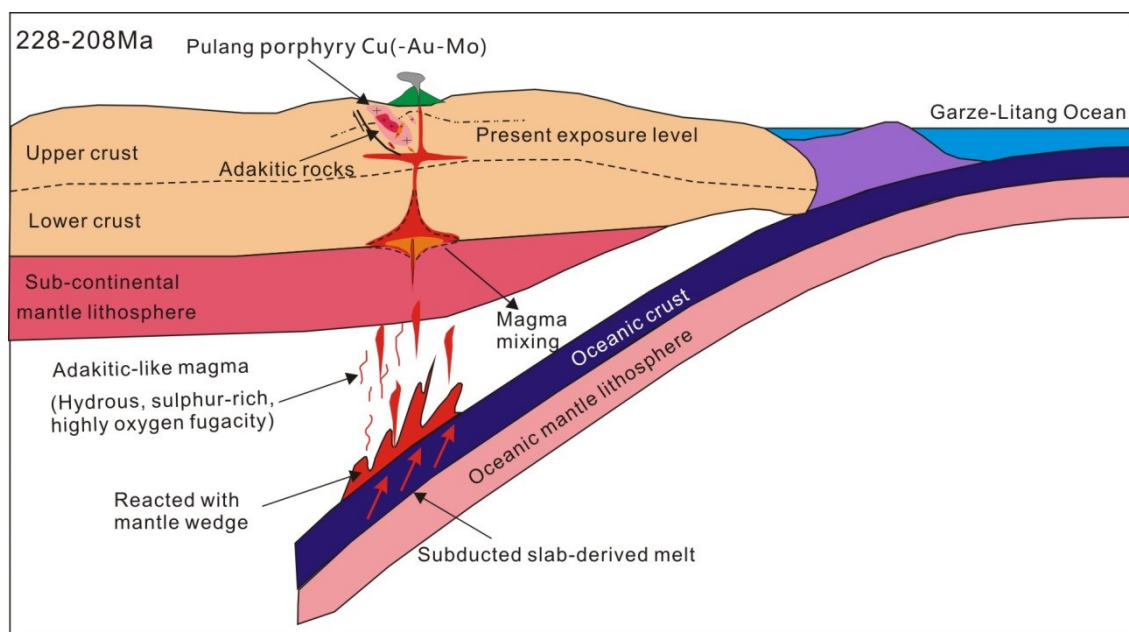


**Figure 13.** Tectonic setting and metallogenic model diagram of the Pulang porphyry Cu (–Mo–Au) deposit.

## 7. Conclusions

According to the LA-ICP-MS zircon U–Pb dating, molybdenite Re–Os dating and whole-rock geochemistry data, the following conclusions can be drawn:

1. Molybdenite from the Pulang porphyry Cu deposit yields the Re–Os age of  $218 \pm 2$  Ma, which is in accordance with most of the porphyry-type Cu deposits in the southern Yidun Arc having mineralization ages of 217–221 Ma. Zircons from the quartz diorite porphyry, quartz monzonite porphyry, and granodiorite porphyry yield U–Pb ages of  $227 \pm 2$  Ma,  $218 \pm 1$  Ma, and  $209 \pm 1$  Ma, respectively, suggesting a close spatial, temporal, and genetical relationship between Cu mineralization and quartz monzonite porphyry.
2. The Pulang porphyry intrusions geochemically belong to high silica (HSA) adakitic rocks. These intrusions derived from the partial melting of subducted Ganzi-Litang oceanic plate that reacted with peridotite during its ascent through the mantle wedge.
3. The Pulang deposit shows similar geological characteristics to the most other porphyry-type Cu deposits in the southern Yidun Arc. These porphyry-type Cu deposits are considered to be related to the westward subduction of the Ganzi-Litang oceanic lithosphere during the Late Triassic.

**Supplementary Materials:** The following are available online at <http://www.mdpi.com/2075-163X/9/3/191/s1>, Table S1: LA-ICP-MS zircon U–Pb dating data of the porphyry intrusions in the Pulang Cu (–Mo–Au) deposit, Table S2: Whole-rock major and trace element data of the porphyry intrusions in the Pulang Cu (–Mo–Au) deposit.

**Author Contributions:** Conceptualization: Q.Y., Y.-S.R., and S.-B.C.; field investigation: Q.Y., G.-L.Z., and Q.-H.Z.; experimental analysis: Y.-J.H.; software: J.-M.L., X.-H.S., Z.-J.Y., and Z.-M.S.; validation: Q.Y. and Y.-S.R.; resources: Y.-S.R. and S.-B.C.; data curation: Q.Y.; writing—original draft preparation: Q.Y.; writing—review & editing: Y.-S.R.; visualization: Q.Y.; funding acquisition: S.-B.C. and Y.-S.R.

**Funding:** This work was financially supported by The Program for Jilin University Science and Technology Innovative Research Team (JLUSTIRT, 2017TD-26), the Industrial Application Projects in Provinces (autonomous regions and cities) of the National High Resolution Earth Observation System Major Science and Technology Project: Black Soil Area Agricultural Information Industrialization Application of High Resolution Special Projects in the Central and Western Jilin (71-Y40G04-9001-15/18), and the Changbai Mountain Scholars Program (440050117009), Jilin Province, China.

**Acknowledgments:** We would like to thank the leaders and geologists of the Pulang ore district for their support of our fieldwork.

**Conflicts of Interest:** The authors declare no conflict of interest.

## References

- Leng, C.-B.; Zhang, X.-C.; Wang, S.-X.; Qin, C.-J.; Gou, T.-Z.; Wang, W.-Q. SHRIMP zircon U–Pb dating of the Songnuo ore–hosting porphyry, Zhongdian, Northwest Yunnan, China and its geological implication. *Geotecton. Metall.* **2008**, *32*, 124–130. (In Chinese)
- Zhang, X.-C.; Leng, C.-B.; Yang, C.-Z.; Wang, W.-Q.; Qin, C.-J. Zircon SIMS U–Pb isotopic age and its significance of ore–bearing porphyry of Chundu porphyry copper deposit in Zhongdian, Northwestern Yunnan. *Acta Miner. Sin.* **2009**, *29*, 359–360. (In Chinese)
- Cao, D.-H. Porphyry Copper Deposit Model and Exploration Technique in Zhongdian, Yunnan. Ph.D. Thesis, Chinese Academy of Geological Sciences, Beijing, China, 2007. (In Chinese)
- Liu, J.-T. Late-Transic Cu Mineralization in Porphyry Environment, Northwest Yunnan, China. Ph.D. Thesis, China University of Geosciences, Beijing, China, 2014. (In Chinese)
- Pang, Z.-S.; Du, Y.-S.; Wang, G.-W.; Guo, X.; Cao, Y.; Li, Q. Single–grain zircon U–Pb isotopic ages, geochemistry and its implication of Pulang complex in Yunnan Province, China. *Acta Petrol. Sin.* **2009**, *25*, 159–165. (In Chinese)
- Liu, X.-L.; Li, W.-C.; Yin, G.-H.; Zhang, N. The geochronology, mineralogy and geochemistry study of the Pulang porphyry copper deposits in Geza arc of Yunnan Province. *Acta Petrol. Sin.* **2013**, *29*, 3049–3064. (In Chinese)
- Leng, C.-B.; Zhang, X.-C.; Hu, R.-Z.; Wang, S.-X.; Zhong, H.; Wang, W.-Q.; Bi, X.-W. Zircon U–Pb and molybdenite Re–Os geochronology and Sr–Nd–Pb–Hf isotopic constraints on the genesis of the Xuejiping porphyry copper deposit in Zhongdian, Northwest Yunnan, China. *J. Asian Earth Sci.* **2012**, *60*, 31–48. [[CrossRef](#)]
- Cao, D.-H.; Wang, A.-J.; Huang, Y.-F.; Zhang, W.; Hou, K.-J.; Li, R.-P.; Li, Y.-K. SHRIMP geochronology and Hf isotope composition of zircons from Xuejiping porphyry copper deposit, Yunnan province. *Acta Geol. Sin.* **2009**, *83*, 1430–1435. (In Chinese)
- Li, W.-C.; Yu, H.-J.; Gao, X.; Liu, X.-L.; Wang, J.-H. Review of Mesozoic multiple magmatism and porphyry Cu–Mo (W) mineralization in the Yidun Arc, eastern Tibet Plateau. *Ore Geol. Rev.* **2017**, *90*, 795–812. [[CrossRef](#)]
- Wang, B.-Q.; Zhou, M.-F.; Li, J.-W.; Yan, D.-P. Late Triassic porphyritic intrusions and associated volcanic rocks from the Shangri–La region, Yidun terrane, Eastern Tibetan Plateau: Adakitic magmatism and porphyry copper mineralization. *Lithos* **2011**, *127*, 24–38. [[CrossRef](#)]
- Chen, J.-L.; Xu, J.-F.; Ren, J.-B.; Huang, X.-X.; Wang, B.-D. Geochronology and geochemical characteristics of Late Triassic porphyritic rocks from the Zhongdian arc, eastern Tibet, and their tectonic and metallogenic implications. *Gondwana Res.* **2014**, *26*, 492–504. [[CrossRef](#)]
- Ren, J.-B.; Xu, J.-F.; Chen, J.-L. Zircon geochronology and geological implications of ore-bearing porphyries from Zhongdian arc. *Acta Petrol. Sin.* **2011**, *27*, 2591–2599. (In Chinese)
- Ren, J.-B.; Xu, J.-F.; Chen, J.-L.; Zhang, S.Q.; Liang, H.Y. Geochemistry and petrogenesis of Pulang porphyries in Sanjiang region. *Acta Petrol. Miner.* **2011**, *30*, 581–592. (In Chinese)

14. Wang, P.; Dong, G.-C.; Zhao, G.-C.; Han, Y.-G.; Li, Y.-P. Petrogenesis of the Pulang porphyry complex, southwestern China: Implications for porphyry copper metallogenesis and subduction of the Paleo-Tethys Oceanic lithosphere. *Lithos* **2018**. [[CrossRef](#)]
15. Zeng, P.-S.; Mo, X.-X.; Yu, X.-H.; Hou, Z.-Q.; Xu, Q.-D.; Wang, H.-P.; Li, H.; Yang, C.-Z. Porphyries and porphyry copper deposits in Zhongdian Area, Northwestern Yunnan. *Miner. Depos.* **2003**, *22*, 394–400. (In Chinese)
16. Li, W.-C.; Zeng, P.-S. Characteristics and metallogenic model of the Pulang superlarge porphyry copper deposit in Yunnan, China. *J. Chengdu Univ. Technol.* **2007**, *34*, 436–446. (In Chinese)
17. Guo, X.; Du, Y.-S.; Pang, Z.-S.; Li, S.-T.; Li, Q. Characteristics of the ore-forming fluids in alteration zones of the Pulang porphyry copper deposit in Yunnan Province and its metallogenic significance. *Geosciences* **2009**, *23*, 465–471.
18. Zeng, P.-S.; Li, W.-C.; Wang, H.-P.; Li, H. The Indoshinian Pulang superlarge porphyry copper deposit in Yunnan, China: Petrology and chronology. *Acta Petrol. Sin.* **2006**, *22*, 989–1000. (In Chinese)
19. Li, W.-C.; Yin, G.-H.; Lu, Y.-X.; Liu, X.-L.; Xu, D.; Zhang, S.-Q.; Zhang, N. The evolution and <sup>40</sup>Ar–<sup>39</sup>Ar isotopic evidence of the Pulang Complex in Zhongdian. *Acta Geol. Sin.* **2009**, *83*, 1421–1429. (In Chinese)
20. Li, W.-C.; Zeng, P.-S.; Hou, Z.-Q.; Zeng, P.-S.; Noel, C.-W. The Pulang Porphyry Copper Deposit and Associated Felsic Intrusions in Yunnan Province, Southwest China. *Econ. Geol.* **2011**, *106*, 79–92.
21. Liu, H.; Zhang, C.-Q.; Jia, F.-D.; Zhou, Y.-M.; Lou, D.-B. Mineral and geochemical evidences of magma-mixing from Pulang porphyry copper deposit in SW Sanjiang, China. *Acta Petrol. Sin.* **2015**, *31*, 3189–3202. (In Chinese)
22. Wang, S.-X.; Zhang, X.-C.; Leng, C.-B.; Qing, J.-C.; Ma, D.-Y.; Wang, W.Q. Zircon SHRIMP U–Pb dating of the Pulang porphyry copper deposit, Northwestern Yunnan, China: The ore-forming time limitation and geological significance. *Acta Petrol. Sin.* **2008**, *24*, 2313–2321. (In Chinese)
23. Yang, Z. Late Triassic mineralization of the porphyry copper deposits in Yidun arc, Southwest China. Ph.D. Thesis, China University of Geosciences, Beijing, China, 2017. (In Chinese)
24. Fan, Y.-H.; Li, W.-C. Geological characteristics of the Pulang porphyry copper deposit, Yunnan. *Geol. China* **2006**, *33*, 352–362. (In Chinese)
25. Zeng, P.-S.; Wang, H.-P.; Mo, X.-X.; Yu, X.; Li, W. Tectonic setting and prospects of porphyry copper deposits in Zhongdian island-arc belt. *Acta Geosci. Sin.* **2004**, *25*, 535–540. (In Chinese)
26. Sun, H.-S.; Li, H.; Martin, D.; Xia, Q.-L.; Jiang, C.-L.; Wu, P.; Yang, H.; Fan, Q.-R.; Zhu, D.-S. U–Pb and Re–Os geochronology and geochemistry of the Donggebi Mo deposit, Eastern Tianshan, NW China: Insights into mineralization and tectonic setting. *Ore Geol. Rev.* **2017**, *86*, 584–599. [[CrossRef](#)]
27. Cao, K.; Xu, J.-F.; Chen, J.-L.; Huang, X.-X.; Ren, J.-B. Origin of porphyry intrusions hosting superlarge Pulang porphyry copper deposit in Yunnan Province: Implications for metallogenesis. *Miner. Depos.* **2014**, *33*, 307–322. (In Chinese)
28. Cao, K.; Yang, Z.-M.; Xu, J.-F.; Fu, B.; Li, W.-K.; Sun, M.-Y. Origin of dioritic magma and its contribution to porphyry Cu–Au mineralization at Pulang in the Yidun arc, eastern Tibet. *Lithos* **2018**. [[CrossRef](#)]
29. Xiao, L.; He, Q.; Pirajno, F.; Ni, P.; Du, J.-X.; Wei, Q.-R. Possible correlation between a mantle plume and the evolution of Paleo-Tethys Jinshajiang Ocean: Evidence from a volcanic rifted margin in the Xiaru-Tuoding area, Yunnan, SW China. *Lithos* **2008**, *100*, 112–126. [[CrossRef](#)]
30. Roger, F.; Jolivet, M.; Malavieille, J. The tectonic evolution of the Songpan-Garzê (North Tibet) and adjacent areas from Proterozoic to Present: A synthesis. *J. Asian Earth Sci.* **2010**, *39*, 254–269. [[CrossRef](#)]
31. Pullen, A.; Kapp, P.; Gehrels, G.E.; Vervoort, J.D.; Ding, L. Triassic continental subduction in central Tibet and Mediterranean-style closure of the Paleo-Tethys Ocean. *Geology* **2008**, *36*, 351–354. [[CrossRef](#)]
32. Hou, Z.-Q.; Yang, Y.-Q.; Qu, X.-M.; Huang, D.-H.; Lü, Q.-T.; Wang, H.-P.; Yu, J.-J.; Tang, S.-H. Tectonic evolution and mineralization systems of the Yidun Arc Orogen in Sanjiang Region, China. *Acta Geol. Sin.* **2004**, *78*, 109–120. (In Chinese)
33. Gao, X.; Yang, L.-Q.; Orovan, E.A. The lithospheric architecture of two subterranean in the eastern Yidun Terrane, East Tethys: Insights from Hf–Nd isotopic mapping. *Gondwana Res.* **2018**, *62*, 127–143. [[CrossRef](#)]
34. Wang, C.-Y.; Li, W.-C.; Wang, K.-Y.; Zhou, X.-B.; Yin, G.-H.; Yu, H.-J.; Xue, S.-R. Characteristics of fluid inclusions and genesis of Xuejiping copper deposit in Northwestern Yunnan Province. *Acta Petrol. Sin.* **2015**, *31*, 967–978. (In Chinese)

35. Reid, A.J.; Wilson, C.J.; Liu, S. Structural evidence for the Permo-Triassic tectonic evolution of the Yidun Arc, eastern Tibetan Plateau. *J. Struct. Geol.* **2005**, *27*, 119–137. [[CrossRef](#)]
36. Yang, T.-N.; Hou, Z.-Q.; Wang, Y.; Zhang, H.-R.; Wang, Z.-L. Late Paleozoic to Early Mesozoic tectonic evolution of northeast Tibet: Evidence from the Triassic composite western Jinsha–Garzê–Litang suture. *Tectonics* **2012**. [[CrossRef](#)]
37. Chen, J.-L.; Xu, J.-F.; Ren, J.-B.; Huang, X.-X. Late Triassic E-MORB-like basalts associated with porphyry Cu-deposits in the southern Yidun continental arc, eastern Tibet: Evidence of slab-tear during subduction? *Ore Geol. Rev.* **2017**, *90*, 1054–1062. [[CrossRef](#)]
38. Hou, K.-J.; Li, Y.-H.; Tian, Y.-R. In situ U–Pb zircon dating using, laser ablation–multiion counting–ICP–MS. *Miner. Depos.* **2009**, *28*, 481–492. (In Chinese)
39. Griffin, W.L.; Powell, W.J.; Pearson, N.J.; O’Reilly, S.Y. GLITTER: Data reduction software for laser ablation ICP–MS. In *Laser Ablation–ICP–MS in the Earth Sciences: Current Practices and Outstanding Issues*; Mineralogical Association Canada Short Course; Sylvester, P., Ed.; Mineralogical Association Canada: Quebec City, QC, Canada, 2008; Volume 40, pp. 308–311.
40. Ludwig, K.R. User’s manual for Isoplot 3.0: A Geochronological Toolkit for Microsoft Excel. *Berkeley Geochronol. Cent. Spec. Publ.* **2003**, *4*, 25–32.
41. Anderson, T. Correction of common lead in U–Pb analyses that do not report <sup>204</sup>Pb. *Chem. Geol.* **2002**, *192*, 59–79. [[CrossRef](#)]
42. Shirey, S.B.; Walker, R.J. Carius tube digestion for low-blank rheniumosmium analysis. *Anal. Chem.* **1995**, *67*, 2136–2141. [[CrossRef](#)]
43. Du, A.-D.; Wu, S.-Q.; Sun, D.-Z.; Wang, S.-X.; Qu, W.-J.; Markey, R.; Stain, H.; Morgan, J.; Malinovskiy, D. Preparation and certification of Re–Os dating reference materials: Molybdenite HLP and JDC. *Geost. Geoanal. Res.* **2004**, *28*, 41–52. [[CrossRef](#)]
44. Smoliar, M.I.; Walker, R.J.; Morgan, J.W. Re–Os ages of group IIA, IIIA, IVA, and IVB iron meteorites. *Science* **1996**, *271*, 1099–1102. [[CrossRef](#)]
45. Hoskin, P.W.O.; Schaltegger, U. The composition of zircon and igneous and metamorphic petrogenesis. *Rev. Miner. Geochem.* **2003**, *53*, 27–62. [[CrossRef](#)]
46. Yang, Q.; Ren, Y.-S.; Sun, Z.-M.; Hao, Y.-J.; Zhang, B.; Sun, X.-H.; Lu, S.-Y. Geochronologic evidence of Late Paleozoic magmatic-hydrothermal mineralization in Tianbaoshan metallogenic region, Yanbian Area: A case study of Xinxing lead-zinc (silver) deposit. *Acta Petrol. Sin.* **2018**, *34*, 3153–3166. (In Chinese)
47. Qiu, K.-F.; Yu, H.-C.; Gou, Z.-Y.; Liang, Z.-L.; Zhang, J.-L.; Zhu, R. Nature and origin of Triassic igneous activity in the Western Qinling Orogen: The Wenquan composite pluton example. *Int. Geol. Rev.* **2018**, *60*, 242–266. [[CrossRef](#)]
48. Geng, J.-Z.; Qiu, K.-F.; Gou, Z.-Y.; Yu, H.-C. Tectonic regime switchover of Triassic Western Qinling Orogen: Constraints from LA-ICP-MS zircon U–Pb geochronology and Lu–Hf isotope of Dangchuan intrusive complex in Gansu, China. *Chem. Erde* **2017**, *77*, 637–651. [[CrossRef](#)]
49. Gou, Z.-Y.; Yu, H.-C.; Qiu, K.-F.; Geng, J.-Z.; Wu, M.-Q.; Wang, Y.-G.; Yu, M.-H.; Li, J. Petrogenesis of ore-hosting diorite in the Zaorendao gold deposit at the Tongren-Xiahe-Hezuo polymetallic district, West Qinling, China. *Minerals* **2019**, *9*, 76. [[CrossRef](#)]
50. Yu, H.-C.; Guo, C.-A.; Qiu, K.-F.; McIntire, D.; Jiang, G.-P.; Gou, Z.-Y.; Geng, J.-Z.; Pang, Y.; Zhu, R.; Li, N.-B. Geochronological and geochemical constraints on the formation of the giant Zaozigou Au-Sb deposit, West Qinling, China. *Minerals* **2019**, *9*, 37. [[CrossRef](#)]
51. Irvine, T.H.; Baragar, W.R.A. A guide to the chemical classification of the common volcanic rocks. *Can. J. Earth Sci.* **1971**, *8*, 523–548. [[CrossRef](#)]
52. Peccerillo, A.; Taylor, A.R. Geochemistry of Eocene calc-alkaline volcanic rocks from the Kastamonu area, Northern Turkey. *Contrib. Miner. Petrol.* **1976**, *58*, 63–81. [[CrossRef](#)]
53. Middlemost, E.A.K. A simple classification of volcanic rocks. *Bull. Volcanol.* **1972**, *36*, 382–397. [[CrossRef](#)]
54. Maniar, P.D.; Piccoli, P.M. Tectonic discrimination of granitoids. *Geol. Soc. Am. Bull.* **1989**, *101*, 635–643. [[CrossRef](#)]
55. Pearce, J.A. Geochemical fingerprinting of oceanic basalts with applications to ophiolite classification and the search for Archean oceanic crust. *Lithos* **2008**, *100*, 14–48. [[CrossRef](#)]
56. Boynton, W.V. Geochemistry of the rare earth elements: Meteorite studies. In *Rare Earth Element Geochemistry*; Henderson, P., Ed.; Elsevier: Amsterdam, The Netherlands, 1984; pp. 63–114.

57. Sun, S.-S.; McDonough, W.F. Chemical and isotopic systematics of oceanic basalts: Implications for mantle composition and processes. *Spec. Publ. Geol. Soc. Lond.* **1989**, *42*, 313–345. [[CrossRef](#)]
58. Yang, Q.; Ren, Y.-S.; Chen, S.-B.; Zhang, G.-L.; Zeng, Q.-H.; Hao, Y.-J.; Sun, X.-H.; Li, J.-M.; Yang, Z.-J.; Sun, Z.-M. Ore-forming fluid evolution and material sources of the giant Pulang porphyry Cu (–Mo–Au) deposit in Northwestern Yunnan, China: Evidence from fluid inclusions and C–H–O–S–Pb isotopes. *J. Geochem. Explor.* **2018**. under review.
59. Hou, Z.-Q.; Qu, X.-M.; Zhou, J.-R.; Yang, Y.-Q.; Huang, Q.-H.; Lv, Q.-T.; Tang, S.-H.; Yu, J.-J.; Wang, H.-P.; Zhao, J.-H. Collision-Orogenic Process of the Yidun Arc in the Sanjiang Region: Record of Granites. *Acta Geol. Sin.* **2001**, *4*, 484–497. (In Chinese)
60. Hou, Z.-Q.; Zaw, K.; Pan, G.-T.; Mo, X.-X.; Xu, Q.; Hu, Y.-Z.; Li, X.-Z. Sanjiang Tethyan metallogensis in SW China: Tectonic setting, metallogenic epochs and deposit types. *Ore Geol. Rev.* **2007**, *31*, 48–87. [[CrossRef](#)]
61. Reid, A.; Wilson, C.J.L.; Shun, L.; Pearson, N.; Belousova, E. Mesozoic plutons of the Yidun Arc, SW China: U/Pb geochronology and Hf isotopic signature. *Ore Geol. Rev.* **2007**, *31*, 88–106. [[CrossRef](#)]
62. Defant, M.J.; Drummond, M.S. Derivation of some modern arc magmas by melting of young subducted lithosphere. *Nature* **1990**, *347*, 662–665. [[CrossRef](#)]
63. Martin, H.; Smithies, R.H.; Rapp, R.; Moyen, J.F.; Champion, D. An overview of adakite, tonalite-trondhjemite-granodiorite (TTG), and sanukitoid: Relationships and some implications for crustal evolution. *Lithos* **2005**, *79*, 1–24. [[CrossRef](#)]
64. Richards, J.P.; Kerrich, B. Adakite-like rocks: Their diverse origins and questionable role in metallogensis. *Econ. Geol.* **2007**, *102*, 537–576. [[CrossRef](#)]
65. Moyen, J.F. High Sr/Y and La/Yb ratios: The meaning of the “adakitic signature”. *Lithos* **2009**, *112*, 556–574. [[CrossRef](#)]
66. Rapp, R.P.; Watson, E.B. Dehydration melting of metabasalt at 8–32-kbar: Implications for continental growth and crust–mantle recycling. *J. Petrol.* **1995**, *36*, 891–931. [[CrossRef](#)]
67. Sen, C.; Dunn, T. Dehydration melting of a basaltic composition amphibolite at 1.5 and 2.0 GPa: Implications for the origin of adakites. *Contrib. Miner. Petrol.* **1994**, *117*, 394–409. [[CrossRef](#)]
68. Qiu, K.-F.; Deng, J.; Taylor, R.D.; Song, K.-R.; Song, Y.-H.; Li, Q.Z.; Goldfarb, R.J. Paleozoic magmatism and porphyry Cu-mineralization in an evolving tectonic setting in the North Qilian Orogenic Belt, NW China. *J. Asian Earth Sci.* **2016**, *122*, 20–40. [[CrossRef](#)]
69. Qiu, K.-F.; Deng, J. Petrogenesis of granitoids in the Dewulu skarn copper deposit: Implications for the evolution of the Paleotethys Ocean and mineralization in Western Qinling, China. *Ore Geol. Rev.* **2017**, *90*, 1078–1098. [[CrossRef](#)]
70. Stern, C.R.; Killian, R. Role of the subducted slab, mantle wedge and continental crust in the genesis of adakites from the Andean Austral Volcanic Zone. *Contrib. Miner. Petrol.* **1996**, *123*, 263–281. [[CrossRef](#)]
71. Castillo, P.R.; Janney, P.E.; Solidum, R.U. Petrology and geochemistry of Camiguin Island, southern Philippines: Insights to the source of adakites and other lavas in a complex arc setting. *Contrib. Miner. Petrol.* **1999**, *134*, 33–51. [[CrossRef](#)]
72. Kay, S.M.; Mpodozis, C. Magmatism as a probe to the Neogene shallowing of the Nazca plate beneath the modern Chilean flat-slab. *J. S. Am. Earth Sci.* **2002**, *15*, 39–57.
73. Pe-Piper, G.; Piper, J.W. Miocene magnesian andesites and dacites, Evia, Greece: Adakites associated with subducting slab detachment and extension. *Lithos* **1994**, *31*, 125–140. [[CrossRef](#)]
74. Atherton, M.P.; Petford, N. Generation of sodium-rich magmas from newly underplated basaltic crust. *Nature* **1993**, *362*, 144–146. [[CrossRef](#)]
75. Condie, K.C. TTGs and adakites: Are they both slab melts? *Lithos* **2005**, *80*, 33–44. [[CrossRef](#)]
76. Rapp, R.P.; Shimizu, N.; Norman, M.D.; Applegate, G.S. Reaction between slab-derived melts and peridotite in the mantle wedge: Experimental constraints at 3.8 GPa. *Chem. Geol.* **1999**, *160*, 335–356. [[CrossRef](#)]
77. Kelemen, P.B.; Hanghøj, K.; Greene, A.R. One view of the geochemistry of subduction-related magmatic arcs, with an emphasis on primitive andesite and lower crust. *Treatise Geochem.* **2014**, *4*, 749–806.
78. Gill, J.B. *Orogenic Andesites and Plate Tectonics*; Springer: New York, NY, USA, 1981; pp. 1–392.
79. Martin, H. Effect of steeper Archean geothermal gradient on geochemistry of subduction-zone magmas. *Geology* **1986**, *14*, 753–756. [[CrossRef](#)]
80. Pearce, J.A.; Harris, N.B.W.; Tindle, A.G. Trace element discrimination diagrams for the tectonic interpretation of granitic rocks. *J. Petrol.* **1984**, *25*, 956–983. [[CrossRef](#)]

81. Pearce, J.A. Sources and settings of granitic rocks. *Episodes* **1996**, *19*, 120–125.
82. Harris, N.B.W.; Pearce, J.A.; Tindle, A.G. Geochemical characteristics of collision-zone magmatism. *Geol. Soc. Lond. Spec. Publ.* **1986**, *19*, 67–81. [[CrossRef](#)]
83. Sun, W.-D.; Zhang, H.; Ling, M.-X.; Ding, X.; Chung, S.-L.; Zhou, J.-B.; Yang, X.-Y.; Fan, W.-M. The genetic association of adakites and Cu–Au ore deposits. *Int. Geol. Rev.* **2011**, *53*, 691–703. [[CrossRef](#)]
84. Sun, W.-D.; Ling, M.-X.; Chung, S.-L.; Ding, X.; Yang, X.-Y.; Liang, H.-Y.; Fan, W.-M.; Richard, G.; Yin, Q.-Z. Geochemical Constraints on Adakites of Different Origins and Copper Mineralization. *Geol. J.* **2012**, *120*, 105–120. [[CrossRef](#)]
85. Mungall, J.E. Roasting the mantle: Slab melting and the genesis of major Au and Au-rich Cu deposits. *Geology* **2002**, *30*, 915–918. [[CrossRef](#)]
86. Qiu, K.-F.; Yang, L.-Q. Genetic feature of monazite and its U–Th–Pb dating: Critical considerations on the tectonic evolution of Sanjiang Tethys. *Acta Petrol. Sin.* **2011**, *27*, 2721–2732. (In Chinese)
87. Qiu, K.-F.; Li, N.; Taylor, R.D.; Song, Y.-H.; Song, K.-R.; Han, W.-Z.; Zhang, D.-X. Timing and duration of metallogeny of the Wenquan deposit in the West Qinling, and its constraint on a proposed classification for porphyry molybdenum deposits. *Acta Petrol. Sin.* **2014**, *30*, 2631–2643. (In Chinese)
88. Qiu, K.-F.; Song, K.-R.; Song, Y.-H. Magmatic-hydrothermal fluid evolution of the Wenquan porphyry molybdenum deposit in the north margin of the Western Qinling, China. *Acta Petrol. Sin.* **2015**, *31*, 3391–3404. (In Chinese)
89. Qiu, K.-F.; Taylor, R.D.; Song, Y.-H.; Yu, H.-C.; Song, K.-R.; Li, N. Geologic and geochemical insights into the formation of the Taiyangshan porphyry copper–molybdenum deposit, Western Qinling Orogenic Belt, China. *Gondwana Res.* **2016**, *35*, 40–58. [[CrossRef](#)]
90. Qiu, K.-F.; Marsh, E.; Yu, H.-C.; Pfaff, K.; Gulbransen, C.; Gou, Z.-Y.; Li, N. Fluid and metal sources of the Wenquan porphyry molybdenum deposit, Western Qinling, NW China. *Ore Geol. Rev.* **2017**, *86*, 459–473. [[CrossRef](#)]
91. Oyarzun, R.; Marquez, A.; Lillo, J.; Lopez, I.; Rivera, S. Giant versus small porphyry copper deposits of Cenozoic age in northern Chile: Adakitic versus normal calcalkaline magmatism. *Miner. Depos.* **2001**, *36*, 794–798. [[CrossRef](#)]
92. Sun, W.-D.; Bennett, V.C.; Eggins, S.M.; Arculus, R.J.; Perfit, M.R. Rhenium systematics in submarine MORB and back-arc basin glasses: Laser ablation ICP-MS results. *Chem. Geol.* **2003**, *196*, 259–281. [[CrossRef](#)]
93. McDonough, W.F.; Sun, S.S. The composition of the earth. *Chem. Geol.* **1995**, *120*, 223–253. [[CrossRef](#)]



© 2019 by the authors. Licensee MDPI, Basel, Switzerland. This article is an open access article distributed under the terms and conditions of the Creative Commons Attribution (CC BY) license (<http://creativecommons.org/licenses/by/4.0/>).